NTNU
Norwegian University of
Science and Technology

Strain-Path Changes in Brass (Cu-20Zn)

Tonje Asklund Hågensen

Materials Science and Engineering
Submission date: June 2017
Supervisor: Bjørn Holmedal, IMA
Co-supervisor: Jisheng Qin, IMA

Norwegian University of Science and Technology
Department of Materials Science and Engineering

Preface

Master’s thesis carried out at the Department of Materials Science and Engineering (IMA) at The Norwegian University of Science and Technology (NTNU) in Trondheim, from January to June 2017.

The present work is a continuation of the specialization project written by the same author, concerning strain-path changes in low brass (Hågensen, 2016). I am very happy that I got to work more with this topic, and think that I have found some interesting results that needs to the investigated further.

I would like to thank my supervisor Bjørn Holmedal and co-supervisor Jisheng Qin for help and guidance throughout the process. I would also like to thank Pål Skaret for helping me with the mechanical testing, Kai Zhang for letting me use his software for calculations, and the people at the work shop for cutting my samples in a timely manner.

Trondheim, June 2017

Tonje A. Hågensen

Abstract

Metals are often exposed to multi-path loading in the forming process. Plastic deformed in more than one direction can have significant effects on microstructural evolution and mechanical behaviour. These mechanisms and behaviours are not completely understood at the present time, and needs to be investigated further and be incorporated in the current plasticity models.

The intention of this work is to investigate the mechanical effects of strain-path changes, with different deformation modes and amounts of prestrain, for brass plates containing 80% Cu and 20% Zn. Two-step tensile tests with prestrain to 8% were performed for various angles of path change. Compression prestrain with subsequent tensile tension was performed with prestrains of 2% and 4%. Lastly, rolling prestrain to 4.6% and 9.7% with subsequent tension was performed at various angles of path change.

The loading modes had a large influence on the observed effects of strain path changes in Cu-20Zn. Prestrain by rolling and compression showed distinct Bauschinger effects, however, unlike compression prestrain, rolling prestrain also reduced the strain hardening rate. The two-step tensile tests showed permanently increased yield strengths upon reloading. Strain hardening plots of the subsequent loadings all had characteristics indicating substantial deformation twinning. This and other microstructural deformation mechanisms related to strain path changes are discussed with background in the state of the initial brass plates and related observations found in the literature.

Sammendrag

Metaller blir ofte utsatt for flere deformasjonstrinn ved metallforming. Plastisk deformasjon i mer enn én retning kan ha signifikante effekter på mikrostrukturell utvikling og mekaniske egenskaper. Disse effektene og mekanismene er ikke fullstendig forstått, og må derfor undersøkes videre for å inkluderes i dagens plastisitetsmodeller.

Hensikten med dette arbeidet er å undersøke de mekaniske effektene av endringer i tøyningsvei, med ulike deformasjonsmoduser og tøyningsverdier, for messingplater som inneholder 80% Cu og 20% Zn. To-trinns strekkprøver med første tøyning til 8% ble utført for ulike vinkler mellom de to tøyningsretningene. Første tøyningsvei i kompresjon, med påfølgende strekkspenning, ble utført med kompresjonstøyninger på 2% og 4%. Til slutt ble valsing til 4,6% og 9,7% etterfulgt av tøyning i strekk utført med ulike vinkler mellom tøyningsretningene.

Effektene av tøyningsveis-endring i Cu-20Zn ble i stor grad påvirket av deformasjonsmodusene. Valsing og kompresjon etterfulgt av strekktesting viste tydelige Bauschinger-effekter. I motsetning til kompresjon reduserte valsede fortøyninger arbeidsherdingsraten. To-trinns strekkprøver viste permanent økning i flytespenning. Arbeidsherdingsratene av de påfølgende strekktestene hadde alle karakteristikker som indikerte betydelig tvillingdannelse. Denne og andre mikrostrukturelle deformasjonsmekanismer relatert til tøyningsvei-endring ble diskutert med bakgrunn i tilstanden til utgangsmaterialet og relaterte observasjoner fra litteraturen.

Contents

1 Introduction

When a metal is plastically deformed in more than one direction, this can have significant effects on microstructural evolution and mechanical behaviour. When a strain-path change is introduced the flow stress deviates from what is observed for monotonic loading. A metal is often exposed to multi-path loading in the forming process. During deep-drawing, equal channel angular extrusion and spinning, the metal might experience strain-path changes that affect the mechanical properties of the finished metal parts. The microstructural mechanisms and associated mechanical behaviours of strain-strain path changes in metals are not completely understood at the present time, and needs to be investigated further to be incorporated in the current plasticity models.

IF steel and aluminium alloys are relatively sensitive to strain-path changes, and are widely studied in the literature (Barlat et al., 2003b, Bate et al., 2007, Doucet and Wagoner, 1987, Mánik et al., 2015). These metals have high stacking fault energies (SFE). Also, some metals with low SFE are widely studied, e.g. brass and austenitic steels (Hutchinson et al., 1976, Sakharova et al., 2009, Sakharova et al., 2008, Karaman et al., 2002). Strain path changes tend to either increase or lower the yield stress of the material compared to the strength it has in monotonic loading. In addition to stress-strain curves, the work-hardening response can be an indicator of the microstructural evolutions (Vieira et al., 1990, Corrêa et al., 2002).

There is some uncertainty about the reasons for the observed effects of strain-path changes. The first strain-path induce some type of anisotropy in the material. The current explanations evolve largely around the behaviour of dislocation structures. During monotonic strain dislocations tangle and form cells, which are connected to the active slip systems (Gracio et al., 1989). When the strain direction is changed, new slip systems are activated and interact with the previous dislocation walls (Fernandes and Schmitt, 1983, Gracio et al., 1989). For metals with low stacking SFE, twinning is a competing deformation mechanism with dislocation slip. The role of twin development and its interactions with dislocations after path change is not well understood.

The intention of this work is to investigate the mechanical effects of strain-path changes, with different deformation modes and amounts of prestrain, for Cu-20Zn. The present investigations can be regarded as a continuation of the work by Hågensen (2016), which investigated the preparation techniques and annealing parameters for Cu-20Zn, and mechanically tested orthogonal and reverse strain path changes for the material. Orthogonal strain-path changes were induced by two-step tensile sequences, and reverse strain-path changes were induced by compression, with subsequent tensile tension. These results were compared with the mechanical testing carried out in this work, which includes strain-path changes by rolling prestrain and subsequent tensile tension. The same brass plates and the same annealing procedure was used in the present work as in the work by Hågensen (2016).

2 Theory

2.1 Plastic deformation

Plastic deformation of materials is an irreversible deformation due to permanent atomic displacement, as opposed to elastic deformation which is reversible and only includes the stretching of atomic bonds. Metals mainly deform plastically by the movement of dislocations, but for metals with lower stacking fault energies (SFE) twinning as also an important deformation mechanism. Deformation behaviour in uniaxial tension can be presented by stress-strain curves, and by a yield surface for more complex loading.

2.1.1 Stress-strain relationship

When a metal is monotonically deformed, the stress-strain behaviour will typically have similar characteristics to the curve illustrated in Figure 2.1 Material deformation transitions from elastic to plastic at the yield stress, σ_Y. The accurate stress state of yielding is difficult to measure, and the stress value of 0.2% plastic strain is typically used, i.e. $R_{p0.2}$. When a metal is deformed plastically, dislocations move along slip planes and pile up at obstacles such as grain boundaries. When dislocation density increases, the stress required for further plastic deformation increases, and this is known as strain hardening.

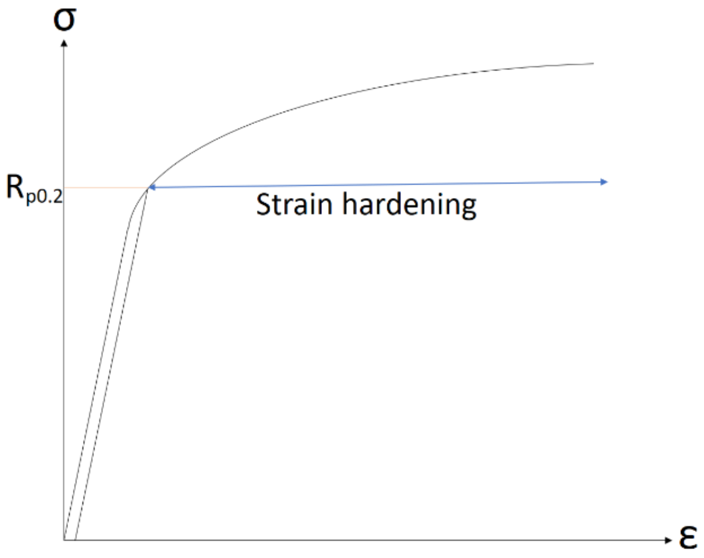

Figure 2.1: Schematic illustration of a stress-strain curve.

Nominal stress and strain are defined as

$$S = \frac{P}{A_0} \tag{1}$$

and

$$e = \frac{\Delta L}{L_0} \tag{2}$$

where P is the force applied, A_0 is the initial cross-sectional area, ΔL is the change in specimen length, and L_0 is the initial specimen length. True stress and strain take into account the change in cross-sectional area that occurs during deformation, and is defined as

$$\sigma = \frac{P}{A_i} \tag{3}$$

and

$$\varepsilon = ln\frac{L_i}{L_0} \tag{4}$$

where A_i is the instantaneous cross-sectional area, L_i is the instantaneous length, and L_0 is the initial length. Nominal stress and strain can be converted to true stress and strain by the relationships

$$\sigma = S(1 + e) \tag{5}$$

and

$$\varepsilon = ln(1 + e) \tag{6}$$

In three dimensions, the strain rate can be represented by a symmetric second order strain tensor

$$\varepsilon_{ij} = \begin{pmatrix} \varepsilon_{11} & \varepsilon_{12} & \varepsilon_{13} \\ \varepsilon_{21} & \varepsilon_{22} & \varepsilon_{23} \\ \varepsilon_{31} & \varepsilon_{32} & \varepsilon_{33} \end{pmatrix} \tag{7}$$

The plastic strain can be found from the total strain value by subtracting the elastic strain, which can be found by the yield strength and Young’s modulus E. Poisson’s ratio ν is the ratio between transverse and axial strain.

2.1.2 Yield surface

The yield surface is used to represent the yielding conditions for stress states in three dimensions. The surface is a cylinder demarcating the inner non-yielded regions from the yielding at the surface, with axis $\sigma_{11} = \sigma_{22} = \sigma_{33}$. The surface expands as the material expands. The yield surface is typically presented in the σ_{11}-σ_{22} plane (with all other stress components zero), as illustrated in Figure 2.2.

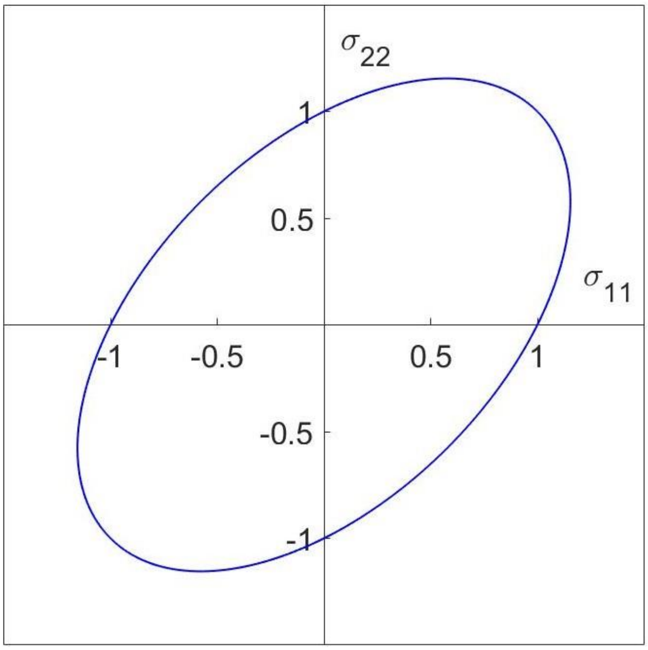

Figure 2.2: Schematic illustration of a yield locus in two dimensions.

The yield function is generally identified by the yield stresses and the *r*-values. Several yield functions have been proposed over the years, i.e. Hill (1948), Hosford (1985), Hill (1990) and Barlat et al. (1997). Tresca (1864), Von Mises (1913), and the yield function proposed by Hershey (1954) are valid for isotropic behaviours. Many plastic anisotropy theories are available, and one of them considers a linear transformation of the stress tensor. Barlat et al. (2003a) proposed an anisotropic yield function (Yld2000-2d), where eight independent anisotropy coefficients were used in the formulation. Setting all anisotropy coefficients in Yld2000-2d equal to 1 recovers the isotropic function proposed by Hershey (1954).

Barlat et al. (2005) proposed a yield surface that was similar to Yld2000-2d, only it was also able to describe the anisotropy of materials subject to three-dimensional stress states. Yld2004-18d contains 18 parameters that accurately describes the material anisotropy when large numbers of experimental data are available. The determination of all the coefficients, uniaxial data from seven different directions between RD and TD are needed, as well as the corresponding r-values, and balanced biaxial data.

An isotropic yield function, independent of isotropic pressure, can be generalized as

$$\phi = \phi(S) = h(\bar{\varepsilon}) \tag{8}$$

where S represents the principal value of the stress deviator s, and h is a hardening function of the accumulated plastic strain $\bar{\varepsilon}$. The stress deviator is the part of the stress tensor that is not related to hydrostatic stress, and which tends to distort the deformed material. The tensor $\tilde{s}$ is defined as a liner transformation of s, according to the equation

$$\tilde{s} = Cs = CT\sigma \tag{9}$$

C is a matrix containing constant anisotropy coefficients, σ is the Cauchy stress tensor, and T transforms σ to its deviator s. The matrixes of C and T are defined as

$$C = \begin{bmatrix} 0 & -c_{12} & -c_{13} & 0 & 0 & 0 \\ -c_{21} & 0 & -c_{23} & 0 & 0 & 0 \\ -c_{31} & -c_{32} & 0 & 0 & 0 & 0 \\ 0 & 0 & 0 & c_{44} & 0 & 0 \\ 0 & 0 & 0 & 0 & c_{55} & 0 \\ 0 & 0 & 0 & 0 & 0 & c_{66} \end{bmatrix} \tag{10}$$

and

$$T = \frac{1}{3}\begin{bmatrix} 2 & -1 & -1 & 0 & 0 & 0 \\ -1 & 2 & -1 & 0 & 0 & 0 \\ -1 & -1 & 2 & 0 & 0 & 0 \\ 0 & 0 & 0 & 3 & 0 & 0 \\ 0 & 0 & 0 & 0 & 3 & 0 \\ 0 & 0 & 0 & 0 & 0 & 3 \end{bmatrix} \tag{11}$$

where c_{ij} are coefficients describing the material anisotropy. For Yld2004-18p two linear transformations, $\tilde{s}'$and $\tilde{s}''$, of s are used,

$$\tilde{s}' = C's' = C'T\sigma \tag{12}$$

and

$$\tilde{s}'' = C''s'' = C''T\sigma \tag{13}$$

The analytical yield function Yld2004-18d is then defined as

$$\begin{aligned}\phi = \phi(\boldsymbol{\Sigma}) = \phi(\tilde{\boldsymbol{S}}', \tilde{\boldsymbol{S}}'') \\ &= \left|\tilde{S}'_1 - \tilde{S}''_1\right|^a + \left|\tilde{S}'_1 - \tilde{S}''_2\right|^a + \left|\tilde{S}'_1 - \tilde{S}''_3\right|^a + \left|\tilde{S}'_2 - \tilde{S}''_1\right|^a \\ &+ \left|\tilde{S}'_2 - \tilde{S}''_2\right|^a + \left|\tilde{S}'_2 - \tilde{S}''_3\right|^a + \left|\tilde{S}'_3 - \tilde{S}''_1\right|^a + \left|\tilde{S}'_3 - \tilde{S}''_2\right|^a \\ &+ \left|\tilde{S}'_3 - \tilde{S}''_3\right|^a = 4\bar{\sigma}^a\end{aligned} \tag{14}$$

where a is the yield exponent. The Yld2004-18d function is described in more detail by Barlat et al. (2005).

2.1.3 R-value

Anisotropy in a material is characterized by the r-value (plastic strain ratio) (Lankford et al., 1950), and is defined by

$$R = \frac{\varepsilon_w^p}{\varepsilon_t^p} \tag{15}$$

where ε_w^p and ε_t^p are the plastic strain in the width and thickness, respectively. If there is anisotropy in the material, the r-value deviates from 1, and the shape of the yield surface is altered. By assuming volume preservation, the r-value can be extended to

$$R = \frac{\varepsilon_w^p}{\varepsilon_t^p} = \frac{\varepsilon_w^p}{-\left(\varepsilon_w^p + \varepsilon_l^p\right)} \tag{16}$$

where ε_l^p is the longitudinal plastic strain. The r-value is usually found by the slope of the ε_w-ε_t curve or ε_w-ε_l curve.

2.1.4 Dislocation structures

The dislocation density increases during plastic deformation of a metal. Dislocations act as obstacles to further deformation, and therefore increase the strength of the metal. As more slip systems are activated, cross slip eventually takes place and multiplication processes operate. At small strains, the microstructural evolution progresses by the formation of low-energy dislocation structures in which neighbouring dislocations mutually screen their stresses, as shown in Figure 2.3a. The structures further develop into dislocation cell blocks within the grains (Figure 2.3b). The cell blocks are delineated by dislocation dense boundaries, that accommodates lattice misorientations resulting from different slip system combinations in neighbouring blocks. The cell blocks are in turn subdivided into ordinary cells. Both cell blocks and ordinary cells shrink in size with increasing strain levels.

The arrangement of the cell walls show close relation to the active slip systems, and the cell shapes are related to the number of active slip planes (Kawasaki and Takeuchi, 1980, Ikeda, 1972). For polycrystalline materials, the interactions between grains might impose internal stresses that lead to multiple slip inside grains, whatever their orientation.

Factors affecting the development of dislocation structures are strain magnitude, grain size, crystallinity, and the interaction between grains. Texture is an important parameter for the formation of dislocation structures as it controls the slip directions.

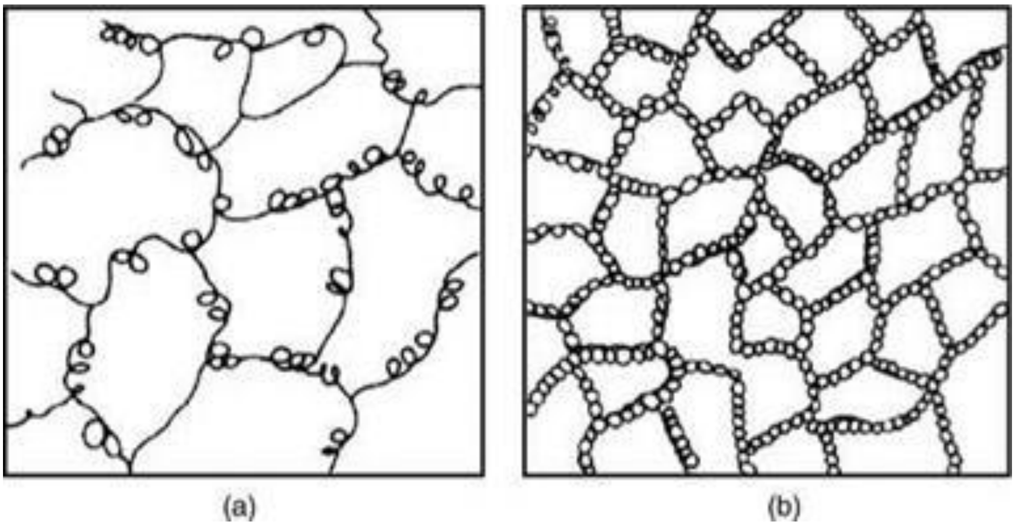

Figure 2.3: Schematic illustration of (a) the beginning cell formation of dislocation structures, and (b) ordinary dislocation cells. (Dieter, 1961)

2.1.5 Twinning

A twin is an atom structure, separated in two parts by a twin boundary, that are located in mirror positions to each other. Twins may be formed by mechanical deformation, or as the result of the annealing process. Annealing twins are produced during recrystallization. Most FCC metals form annealing twins, and their presence is an indicator that the metal has been mechanically deformed prior to annealing, since annealing twins are likely to grow from twin nuclei produced during deformation. These twins are formed as straight lines parallel to the ⟨111⟩ planes. The twin boundaries of annealing twins have about 5 % of the energy of average grain boundaries.

In FCC metals, dislocation movement and twinning are two competing deformation mechanisms, and deformation twinning is especially abundant in metals with low SFE. The two deformation mechanisms differ in several respects. Twinning results in an orientation difference across the twin plane, while slip leaves the crystal above and below the slip plane in the same orientations. Slip is usually considered to occur in discrete multiples of the atomic spacing, while the atomic movement is much less than an atomic spacing for twinning. Slip usually occurs on widely spread slip planes, while in the twinned region every atomic plane is involved in the deformation, as illustrated in Figure 2.4.

The initiation of deformation twins is dependent upon the critical resolved shear stresses for twinning and slip (Chaparro and Fernandes, 2002, Christian and Mahajan, 1995, Vieira et al., 2004). For most materials, deformation twinning does not occur until deformation by dislocation slip has reached a certain level (Chaparro et al., 2004, Christian and Mahajan, 1995, Lee and Lin, 2002). Deformation twins are produced by a shear force, and tend to be lens shaped as a result of the elastic strain in the material related to the formation of these twins.

Twin formation can alter the mechanical properties of metals, as the crystal orientation is changed, and twin boundaries may function as obstacles to dislocation movement. When crystal orientations change, new slip systems might be placed in a favourable orientation with respect to the stress orientation. However, only a relatively small amount of the total crystal volume is reoriented by twinning.

De-twinning is the reorientation of twins back to their original orientation. The stress required for de-twinning is larger than the stress required for twinning, but smaller than the stress required for nucleation, and hence de-twinning is preferred over creating new twins inside primary twins upon load reversal (Proust et al., 2010).

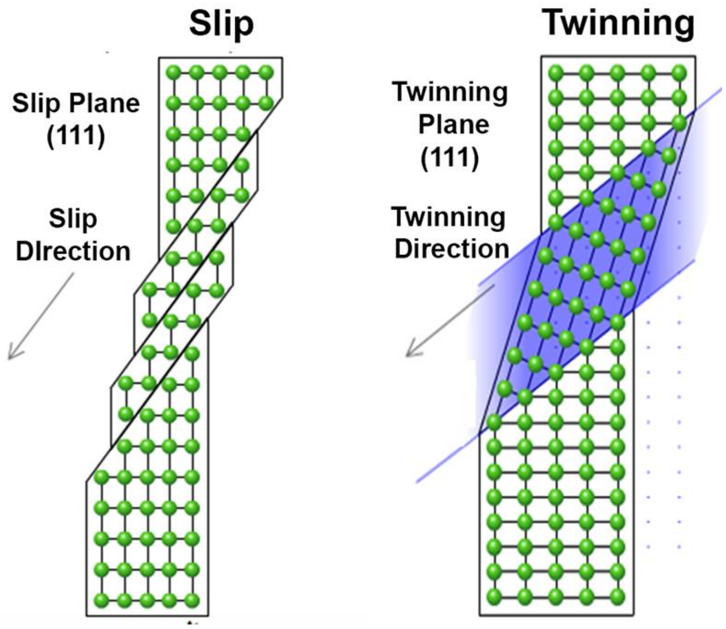

Figure 2.4: Schematic illustration of deformation by slip and twinning in an FCC crystal. (DoITPoMS/University of Cambridge)

2.2 Texture

The texture of a material affects many of its properties, rendering them anisotropic. The yield strength and tensile strength are two examples of such properties. Texture might develop during most stages of material processing, i.e. solidification, deformation, and recrystallization. Textures can be displayed in pole figures or orientation distribution functions (ODF), and are classified as weak, moderate, or strong.

2.2.1 Deformation texture

During plastic deformation of a metal, the grain boundary area increases, and the orientations of the individual grains change. The grain orientations change relative to the loading directions, and result in a preferred texture. Figure 2.5 shows a schematic illustration of a rolled sheet with random texture, and one with very strong cube texture. The deformation mechanisms operating are determining for the microstructure that develops. Deformation by slip is the most dominant mechanism, and lead to rotation of crystals. Twinning lead to abrupt changes in the orientation. As the dislocation density increases with increasing plastic deformation, the misorientations across the dislocation cells also increase.

The amount and nature of textures developed during deformation depend on several factors, such as the crystal structure and its characteristics, initial texture, chemical composition, previous processing, temperature, and strain rate.

The SFE influences the deformation texture formation. By adding alloying elements to copper and other high SFE metals, the SFE is lowered. During deformation by rolling, metals with low SFE typically has a strong brass (B) component {110}⟨112⟩, and a minor Goss (G) component {110}⟨001⟩.

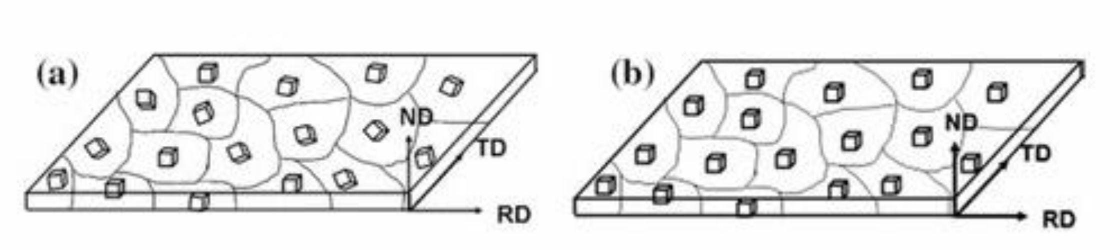

Figure 2.5: Rolled sheet with (a) Random texture, and (b) very strong texture with (100)[010] orientation. (Suwas and Ray, 2014)

2.2.2 Annealing texture

A plastically deformed metal is in a thermodynamically metastable state, due to the energy that is stored in the metal. By increasing the temperature, lattice defects can be removed and rearranged, and the internal energy can be released. The annealing process consists of recovery, recrystallization, and grain growth. When a material is recrystallized, the original deformed texture is replaced by strain free grains.

The annealing texture depend on the orientation dependence of the rate of nucleation, the immediate environment of the nuclei, the nature, energy, and mobility of grain boundaries. The texture before deformation, the amount of deformation strain, material purity, and the extent of grain growth after recrystallization also affects the annealing texture. The texture might be only slightly related, or identical, to the deformation texture, depending on the material and its purity, and the deformation conditions.

Pure copper produces an almost random recrystallization texture when deformed up to 50% (Hu et al., 1966). For deformations above 95% copper recrystallization texture has a strong cube component ({100}⟨001⟩). When zinc is added to the copper, the SFE is gradually lowered, and the deformation texture changes over to that of α-brass. The cube component of the recrystallization texture decreases, and almost completely vanishes at 10 % zinc. Low brass typically form recrystallized brass texture {236}⟨385⟩ after primary recrystallization (Gottstein and Shvindlerman, 2009), however, it is replaced by a grain growth texture

{197}⟨211⟩ after prolonged annealing (Brickenkamp, 1983). This texture is comparable to the brass orientation formed during rolling.

2.2.3 Representation of texture

Pole figures (PF) are two-dimensional stereographic projections of positions and intensities of specific crystallographic orientations, relative to the specimen orientation. Figure 2.6 shows a schematic of the construction of a pole figure. Imagine a reference sphere, so small that it can be considered a point. For rolled plates the reference directions are aligned with the rolling-, transverse-, and normal direction (Figure 2.6a). When looking top down on the projection, the ND will be in the centre, and RD and TD will be on the periphery of the projection (Figure 2.6b). Figure 2.6c-f shows how the three perpendicular planes (100), (010), and (001) are projected. When an area of a specimen is scanned, the different orientation projections will spread out. If the majority of the poles are clustered together, the material has a strong texture. If the poles are distributed rather uniformly, the material has a weak or random texture. The pole densities are often represented by contour lines (Figure 2.6f), where the number against each line represents the density of poles relative to that which would be expected for a random texture. For instance, contour lines representing 1 and 2 times random, which represents a concentration of poles.

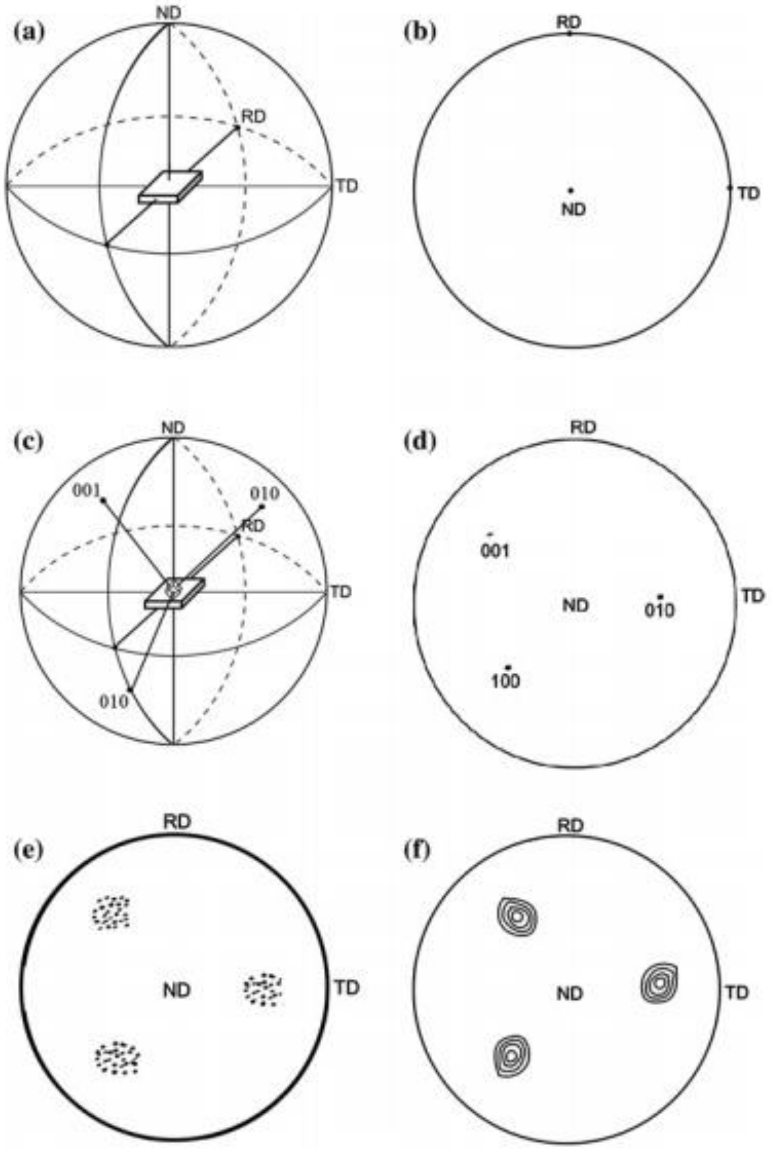

Figure 2.6: (a) A reference sphere and a projection plane with a rolled plate in the centre. (b) Stereographic projection of the RD, TD and ND. (c) Intersections of the (100), (010), and (001) planes with the reference sphere. (d) Stereographic projections of the (100), (010), and (001) poles. (e) Cluster of pole projections as discrete points. (f) Densities of pole projections as contour lines. (Suwas and Ray, 2014)

PF's s are two-dimensional representations of the orientation of a three-dimensional entity, and therefore PF's don't give a sufficient description of texture. An orientation distribution figure (ODF) might be viewed as a collection of PF's, and gives a three-dimensional representation of texture. The ODF is a mathematical function that describes the occurrence frequency of crystallographic orientations, usually defined by the Euler space. The Euler angles describes the transition from the samples reference directions to the crystallographic directions of the individual crystallites with the three angles φ_1, Φ, and φ_2. A single crystal is completely described by a point in a cube with axes φ_1, Φ, and φ_2, i.e. the Euler space, which is usually presented as a series of cross-sections. The orientation of a crystallite g can be written as

$$g = g(\varphi_1, \Phi, \varphi_2) \tag{17}$$

If the volume of a crystallite is denoted dV, and it possesses the orientation g with the spread of dg, then the ODF $f(g)$ can be defined as

$$f(g)dg = \frac{dV}{V} \tag{18}$$

2.2.4 ALAMEL model

Many of the yield functions discussed in chapter 2.1.2 are proven to accurately describe anisotropic behaviour. However, these phenomenological yield functions only consider a small portion of the yield space when fitting the parameters. A different approach to describing anisotropy is by using texture data in polycrystalline plasticity models. The first model to do this was proposed by Sachs (1928), which assumed isotropic stress for all grains in a polycrystal. Later, other models assume that each grain experience the same deformation as the aggregate (full-constraint models) (Bishop and Hill, 1951, Taylor and Quinney, 1932). Some models increased freedom of single grains (relaxed-constraint models) (Kocks and Chandra, 1982, Van Houtte, 1988). Three types of relaxation are shown in Figure 2.7.

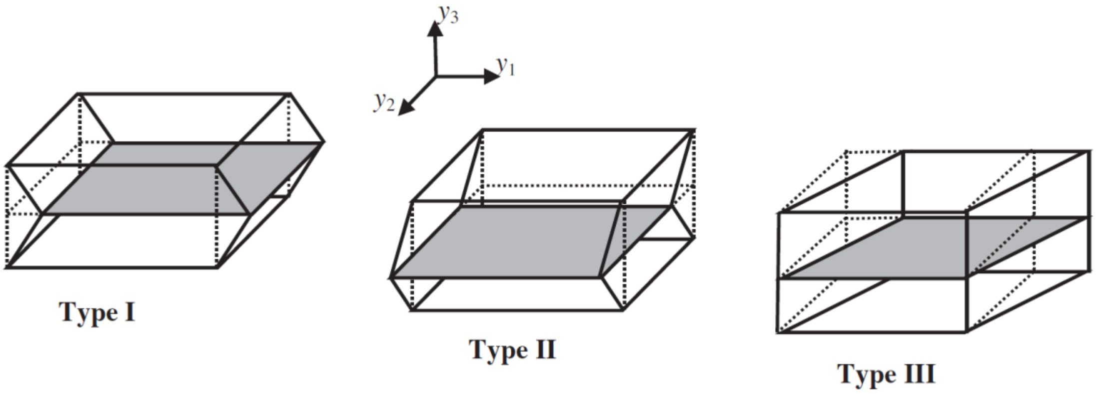

Figure 2.7: Schematic illustration of relaxation type (a) I, (b) II, and (c) III, in the y_1, y_2, y_3 reference frame (Zhang et al., 2015).

The Lamel model is a relaxed-constraint model proposed by Van Houtte et al. (1999) which considers two grains at the same time. Van Houtte et al. (2005) proposed an advanced Lamel model (ALAMEL) which also accounted for grain boundary orientations and general deformation modes. Other types of polycrystalline plasticity models exists but will not be discussed here, i.e. Kröner (1958) and Lebensohn and Tomé (1994).

The ALAMEL model consider two neighbouring grains (grain 1 and 2), which share a grain boundary segment (AB), as illustrated in Figure 2.8. A coordinate system y_1, y_2, y_3 is placed with respect to the macroscopic frame by the Euler angles. The original ALAMEL model finds ALAMEL pairs by randomly selecting crystal orientations from the texture data input. In a more recent model by Zhang et al. (2015) a procedure is proposed to obtain the measured misorientation distribution function. This model also includes type III relaxation, as opposed to the original ALAMEL model which only considers type I and II relaxation.

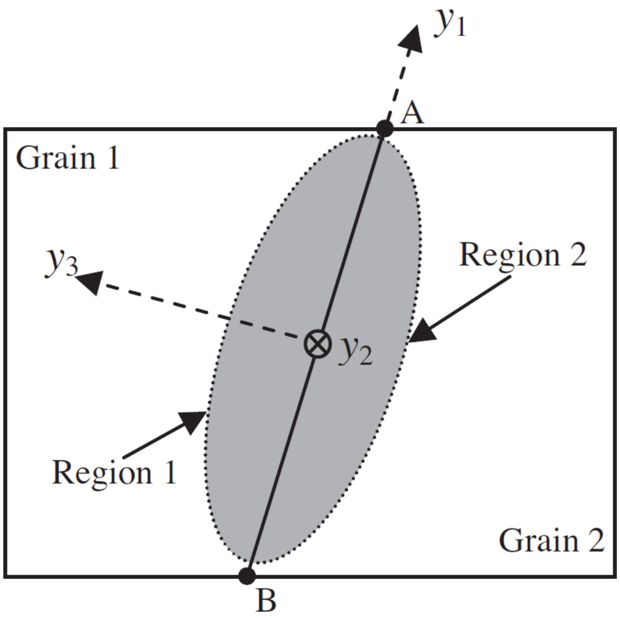

Figure 2.8: Schematic illustration of an ALAMEL pair consisting of the region 1, region 2 and a grain boundary AB, with a coordinate system y_1, y_2, y_3. (Zhang et al., 2015)

2.2.5 Electron backscatter diffraction

Electron backscatter diffraction (EBSD) is a technique for microtexture measurement using scanning electron microscope (SEM). In addition to the latter, EBSD also provides information about other microstructural parameters, such as grain size, phases, and misorientation angle. The EBSD arrangement is shown in Figure 2.9. The electron beam hits the uppermost surface layer of a sample which is tilted 70°, and a fraction of the electrons are backscattered. Some of the backscattered electrons will arrive at the correct Braggs angle for several lattice planes, get diffracted, and create strong beams. A suitably placed phosphor screen detects the reflected beams. The reflected beams have a low Braggs angle, and the angle of the diffraction cones are therefore nearly 180°, and appear flat on the screen. The straight lines detected by the phosphor screen form Kikuchi patterns that in turn are recorded by a camera of CCD device, and the process is repeated for a given number of places over an area. The diffraction patterns are digitalized and analysed by computer processing to find the crystal orientations. Indexing of Kikuchi patterns is done by analysing all possible combinations of bands, and band triplets are used to identify an orientation. Each orientation receives a vote every time it is identified, and the orientation which receives the highest amount of votes in total is chosen as the solution. The Confidence Index (CI) is a parameter used to determine the uniqueness of an individual indexing solution, and it is the difference between the votes received by the two highest ranked solutions, divided by the total possible number of votes. CI lies between 0 (good) and 1 (perfect), but does not have to be 1 for the indexing to be correct.

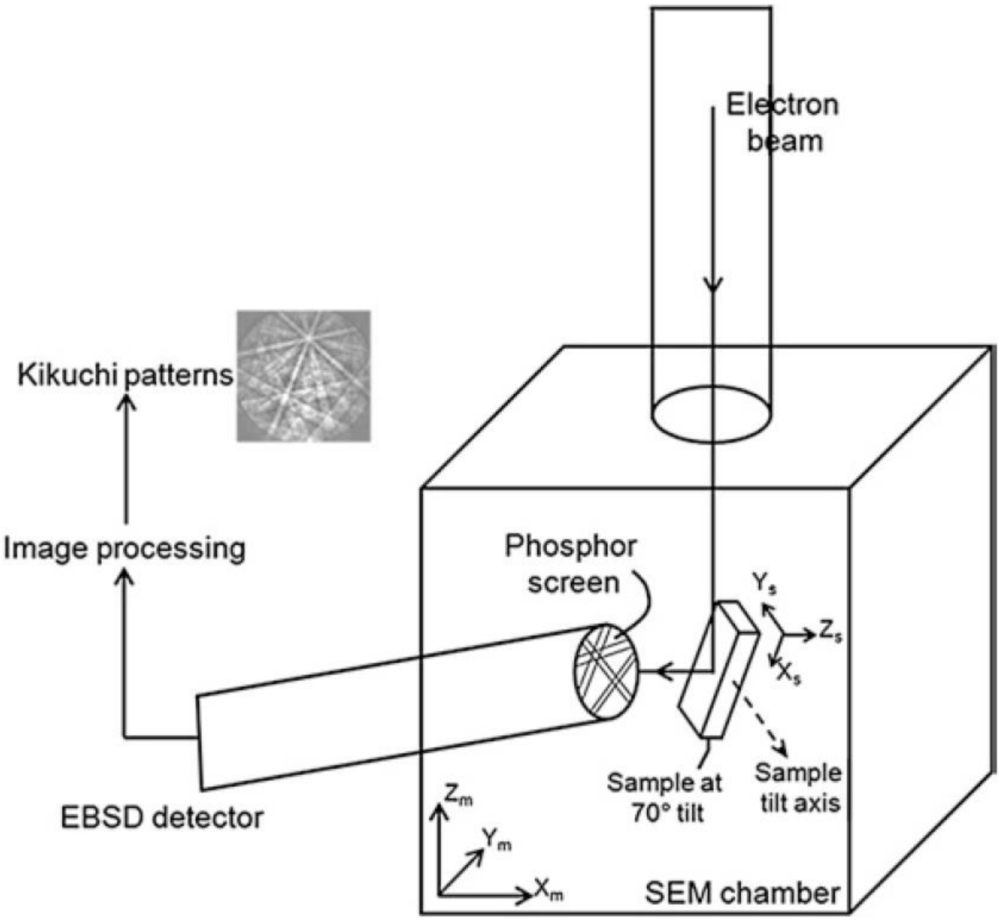

Figure 2.9: Schematic illustration of an EBSD set-up attached to a SEM. (Suwas and Ray, 2014)

2.3 Strain-path change

When the strain path is changed during plastic deformation, the mechanical characteristics tend to change from that of monotonic loading. In the literature, orthogonal and reverse strain path changes are mainly investigated. Strain path changes tend to either increase or lower the yield strength of the material compared to the strength it has in monotonic loading. This is referred to as the Bauschinger effect and cross hardening, respectively.

IF steels and aluminium alloys are examples of metals that are sensitive to strain-path change and are subjects to intensive experimental investigation (Barlat et al., 2003b, Doucet and Wagoner, 1987, Bate et al., 2007). Also metals with low SFE, e.g. brass and austenitic steels, are studied (Hutchinson et al., 1976, Sakharova et al., 2009, Sakharova et al., 2008, Karaman et al., 2002).

2.3.1 Bauschinger effect

The Bauschinger effect (Bauschinger, 1881) is the directionality of strain hardening which leads to the reduction of the yield strength upon reloading. When a material is loaded beyond the yield point in one direction, the yield strength in other directions are reduced. Figure 2.10 shows an illustration of the Bauschinger effect where the yield strength is reduced from σ_Y to σ_Y^*. The Bauschinger effect normally occurs for reverse and pseudo-reverse strain path changes.

A possible explanation of this phenomenon is given by Orowan (1959). When a material is strained in one direction dislocation cells are formed. Upon reloading in the opposite direction, some dislocations move easily at low shear stress since the barriers to the rear are weaker than the ones in front. However, Rauch (1997) found that reverse tests of mild steel with homogeneous dislocation distribution had a 10% lower reloading yield stress than mild steel with a cell structure, and argues that the concentration of dislocations drives the Bauschinger effect rather than cell formation.

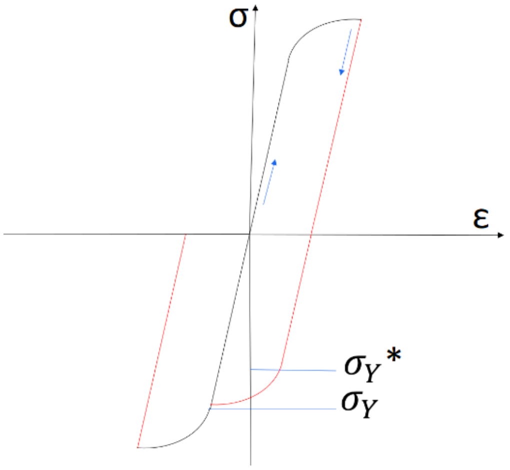

Figure 2.10: Schematic illustration of the Bauschinger effect.

2.3.2 The magnitude of strain-path change

Strain path change can be quantified by the parameter

$$\cos\theta = \frac{\dot{\varepsilon_p} : \dot{\varepsilon}}{\|\dot{\varepsilon}\| \; \|\dot{\varepsilon}\|} \tag{19}$$

where $\dot{\varepsilon_p}$ is the pre-loading strain rate tensor, ε is the subsequent strain rate tensor, and θ is the so-called Schmitt angle (Schmitt et al., 1985). The orientation change between prestrain and subsequent strain characterizes the microstructural effects of a strain path change (Schmitt et al., 1985). Monotonic loading is represented by the value $\theta = 0°$, and hence $\cos\theta = 1$. Orthogonal and reverse strain path change is represented by the values $\cos\theta = 0$ ($\theta = 90°$) and $\cos\theta = -1$ ($\theta = 180°$), respectively.

From equation (19), the Schmitt angle θ (Schmitt et al., 1991) for a two-step tensile test can be calculated as

$$\theta = \cos^{-1}\left(\frac{3 + (1 + 2r_1)(1 + 2r_2)\, cos\, 2\alpha}{4\sqrt{1 + r_1 + r_1^2}\sqrt{1 + r_2 + r_2^2}}\right) \tag{20}$$

where r_1 and r_2 are the r-values in the two respective directions, and α is the angle between the strain directions in the global space. The Schmitt angle for rolling prestrain, i.e. $r_1 = 0$, and subsequent tensile is calculated as

$$\theta = \cos^{-1}\left(\frac{3 + (1 + 2r_2)\, cos\, 2\beta}{4\sqrt{1 + r_2 + r_2^2}}\right) \tag{21}$$

where β is the angle between the two straining directions.

2.3.3 Mechanical behaviour

The mechanical behaviour of strain-path change has been widely investigated (Mánik et al., 2015, Sakharova et al., 2009, Vieira et al., 1990, Vincze et al., 2005). For reverse and pseudo-reverse path changes, the Bauschinger effect is typically observed. For orthogonal path changes, the cross hardening effect is typically observed. The cross hardening effect refers to an initial increase in the yield strength, after which there typically is a softening zone and resumption of work-hardening. This effect can often be measured by the value of the reloading yield stress, which is defined as the back extrapolated stress σ_{be} (Raphanel et al., 1986), relative to the reference stress. The softening zone can lead to instability and early strain localization and necking (Li and Bate, 1991). Especially for larger prestrain values, necking might occur rapidly after reloading (Raphanel et al., 1986, Szczepiński and Miastkowski, 1968).

The strain-hardening rate can be plotted to observe deformation mechanisms operating during strain path changes. For metals with medium-to-high SFE the strain hardening rate is observed to be very high right after reloading, have a rapid decrease to a low value, before eventually stagnating (Mánik et al., 2015, Corrêa et al., 2002, Vieira et al., 1990). Several have found that path changes can produce persistent changes. If the hardening rate is also transiently changed as a result of strain path change, the flow stress will experience a permanent effect.

The strain-hardening rate versus stress is plotted (Kocks-Mecking plots) to reveal deformation mechanisms. Kocks-Mecking plots for single crystals typically show four distinct stages of hardening (Kocks et al., 1981). Stage I exhibits an almost zero hardening rate, stage II exhibits an almost constant hardening rate, stage III exhibits a steady decrease in strain hardening rate, and stage IV exhibits an almost constant hardening rate. The first three stages are associated with single slip, initial stages of multiple slip, and dynamic recovery, respectively. The origin of the fourth stage is not clear at the present time. For polycrystalline FCC metals with medium-to-high SFE, it is reviled that stages I and II are greatly diminished, and thus these metals exhibit only stage III and IV hardening (Mecking and Kocks, 1981).

Asgari et al. (1997) suggested plotting $\left(\frac{d\sigma}{d\varepsilon}\right)/G$ versus $(\sigma_{tw} - \sigma_0)/G$ or ε, where G is the shear modulus and σ_0 is the initial yield strength, for polycrystalline FCC metals with low SFE. σ_0 is subtracted to isolate the contribution for dislocation multiplication from other hardening mechanisms, and $(\sigma_{tw} - \sigma_0)/G$ is an indicator of the dislocation density during deformation (El-Danaf et al., 1999). For instance does solid solutions often contribute significantly to the initial yield strength. El-Danaf et al. (1999) proposed a criterion for the initiation of deformation twinning for polycrystalline FCC metals with low SFE at low homologous temperatures

$$(\sigma_{tw} - \sigma_0)/G = C\left(\frac{d}{b}\right)^A \tag{22}$$

where σ_{tw} is the deformation twinning stress, d is the average homogenous slip length, b is Burgers vector magnitude, and C and A are constants. El-Danaf et al. (1999) also proposed that SFE has only an indirect effect on the twinning stress, contrary to classical studies concluding that the twinning stress has a parabolic dependence on the SFE.

The strain-hardening behaviour of low SFE FCC metals exhibit a four stage response (Asgari et al., 1997) which is quite different from that of metals with moderate-to-high SFE. Figure 2.11 shows a schematic illustration of the different stages and deformation mechanisms related to each step. Stage A is similar to stage III in Kocks-Mecking plots for metals with medium-to-high SFE. Stage B is related to the initiation of primary deformation twinning, and stage D is related to extensive twin intersections.

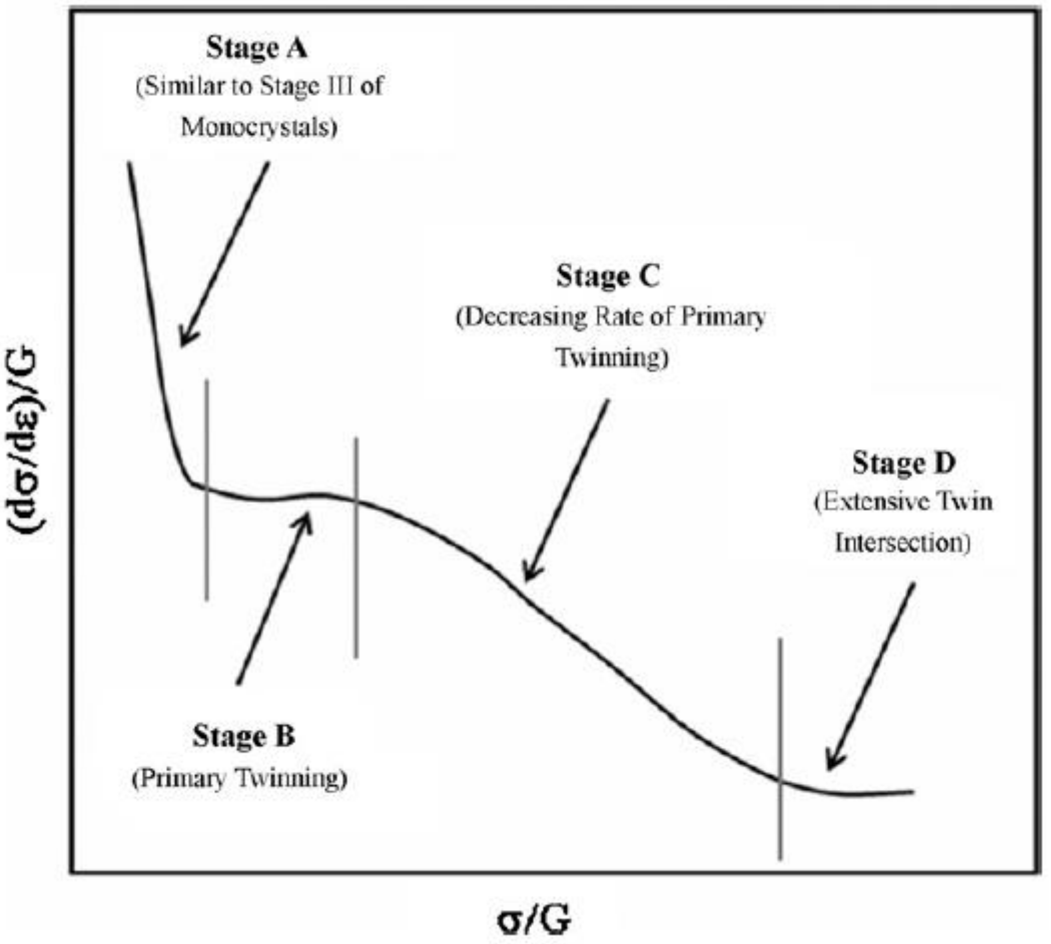

Figure 2.11: Schematic illustration of the typical strain hardening response of metals with low SFE. (Asgari et al., 1997)

2.3.4 Sources for behaviour

At the present time, there is no complete explanation of the microstructural mechanisms that lead to transient responses after strain path changes. Many authors have concluded that development of cell walls is necessary for the transient to occur (Barlat et al., 2003b, Bate et al., 2007, Eardley et al., 2003, Li and Bate, 1991). However, a tress plateau and the Bauschinger effect is also observed for strain-path changes at low temperatures in low carbon steels, where no heterogeneous dislocation distributions were observed (Vincze et al., 2005).

It is believed that the formation of dislocation cells in the material act as a barrier to further plastic deformation. After reloading, active slip systems are observed to change partially or totally, depending of the magnitude of the strain-path change, and cells reorganize, which promotes annihilation of the dislocations (Fernandes and Schmitt, 1983, Gracio et al., 1989). The former dislocation structure is gradually replaced by a new structure, which is more stable under the new conditions.

Deformation twinning is an additional mechanism to dislocation slip that alters the features of deformation. Metals with low-to-moderate SFE tend to deform more by twinning than metals with high SFE. For brass, more twinning is observed under tension after a strain-path change (Sakharova et al., 2009). The development of twinning is observed to lead to a higher work -hardening rate than measured in the absence of twinning (Sakharova et al., 2009), as described in the above chapter. The formation of twins reduces the free slip line distance because the twin-interface acts as a barrier.

Deformation twins are sometimes formed already in prestrain, and are present together with annealing twins, for some materials. After path change, the new slip directions have a different direction in relation to the twin plane, which increases the free slip line distance, and reduce the yield strength (Sakharova et al., 2008). The role of twin interaction with dislocations is an aspect that is not yet well understood.

Increased yield strength after strain path change can also be explained by the latent hardening effect, which is the interaction between newly activated slip systems and slip systems activated during the prestrain. Latent hardening contributes to a higher yield strength, and is a competing mechanism to the increased slip line distance due to dislocation-twin interaction.

Another aspect to consider is the development of shear bands, that play an important role in texture formation and overall hardening rate (Korbel et al., 1983, Ha et al., 2014). Shear bands weakens the material as it holds large stress concentrations. Experiments have shown that heterogeneous deformation modes can be promoted by strain path changes (El-Danaf et al., 2000, Luft, 1991, Thuillier and Rauch, 1994, Wróbel et al., 1996). This can be a temporary effect, or it can lead to shear banding and ultimately failure. The formation of shear bands is strongly influenced by the crystallography and SFE. Metals with low SFE typically form brass type shear bands (Paul et al., 2002), while metals with medium-to-high SFE typically form copper type shear bands (Wróbel et al., 1996, Wagner et al., 1995).

3 Experimental

In this chapter, the experimental procedures for investigating strain path changes with rolling prestrain and subsequent tensile tension, of annealed Cu-20Zn plates, are explained. The brass plates used in this investigation were low brass (Cu-20Zn), which is a single-phase alloy with zinc in solid solution. The low brass is α-brass which has FCC structure and low SFE of 18mJ/m^2 (Loretto et al., 1965). The plates used were previously rolled to an unknown amount, and hence had to be totally recrystallized and investigated with SEM before further experiments were conducted. The plates had a thickness of 1 mm.

3.1 Annealing

To assure total recrystallization of the brass plates they were heat treated in a Nabertherm muffle furnace for 5 hours and 10 minutes, at 600°C. The time and temperature were determined in the work by Hågensen (2016). In the work by Hågensen (2016) an annealing curve was found experimentally by heating specimens at eight different temperatures (25°, 300°, 350°, 400°, 450°, 500°, 550° and 600°) in salt baths, for 30 minutes. One additional specimen was heated in salt bath at 600° for 5 hours. The hardness was tested at three different locations on all specimens, and a drop in the hardness values was observed between 450° and 500°. The specimen annealed for 5 hours at 600° was mechanically polished to 1µm and etched, and the grain structure was studied with optical microscopy. The grain structure appeared to be totally recrystallized, and the remaining brass plates were therefore annealed with the above-mentioned conditions.

3.2 Material characterization

The material preparation procedures of Cu-20Zn in SEM EBSD was found by Hågensen (2016). Smaller specimens were cut out from the large brass plates, grinded and mechanically polished to 1µm, then electropolished using E2 electrolyte with the parameters listed in Table 1. The E2 electrolyte was mixed according to Table 2.

Table 1: Electropolishing parameters.

Parameter	Value
Area	0.5 cm2
Flow rate	10
Temperature	25°
Voltage	20 V
Time	10 sec

Table 2: E2 electrolyte composition.

Chemical	Amount
Copper(II) nitrate	300 g
Methanol	900 ml
Nitric acid	30 ml

The annealed plates were scanned by electron backscatter diffraction (EBSD) in a scanning electron microscope (SEM). The electropolished samples were placed in a Zeiss Ultra 55 LE FESEM, with the surface to be scanned at 70° to the horizontal. The EBSD signals were collected and processed using a Nordif UF1100 detector. The EBSD settings used are listed in Table 3. Five scans were performed and merged together for a total area of 1.4 mm^2. The ND-TD plane of the specimen was scanned, as illustrated in Figure 3.1. Table 3 lists the EBSD settings used for these scans.

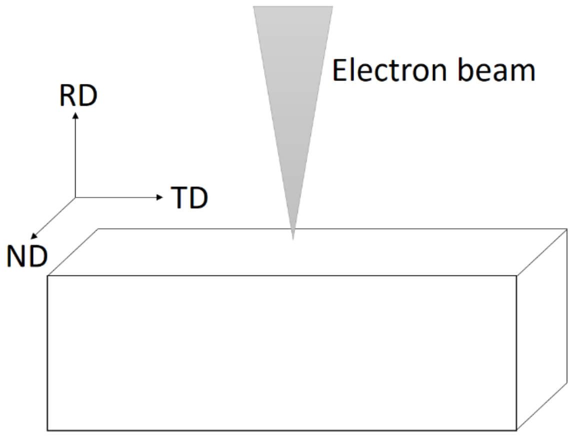

Figure 3.1: EBSD scan setup.

The obtained patterns were indexed by EDAX Orientation Imaging Microscopy (OIM) Data Collection 7 software, and EDAX OIM Analysis software was used for microstructure analysis. In the OIM Analysis software the orientation data was rotated 90° about the TD direction to obtain data in the RD-TD plane.

Table 3: EBSD scan parameters.

Parameter	Value
Accelerating voltage	20kV
Working distance	25.3 mm
Magnification	200
Step size	1.5 µm

3.3 Mechanical testing

To investigate the mechanical effects of strain path changes in low brass (Cu-20Zn), different deformation modes, Schmitt angles and prestrain values were tested. Some of the mechanical testing was performed in the work by Hågensen (2016), including orthogonal strain path change by two step tensile testing, and reverse strain path change by compression and tensile testing. In the present work, the plates were prestrained to rolling and subsequently strained by tensile testing. Tensile testing was used as the subsequent strain path for all modes of prestrain to get comparable stress-strain graphs for comparing the mechanical effects of strain-path changes. Figure 3.2 defines the different strain directions relative to a tensile testing specimen.

The same brass plates were used as those in the work by Hågensen (2016), and the plates were heat treated similarly. Tensile test were carried out to test the consistency between the plates in the current work and the work by Hågensen (2016). Hågensen (2016) performed monotonic tensile testing at different angles relative to the rolling direction to determine the material anisotropy. All the tensile testing was performed with a loading rate of 1mm/min, in similar environments.

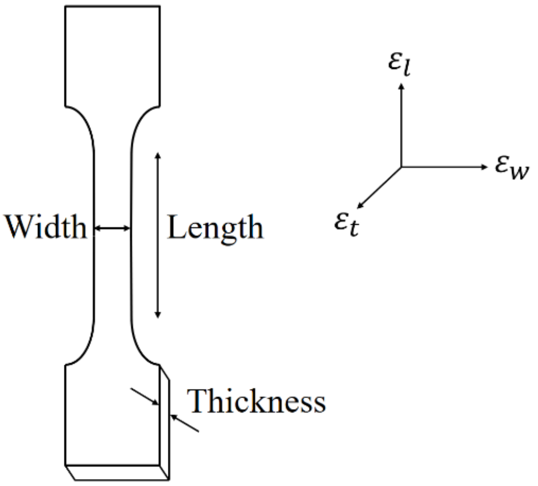

Figure 3.2: Schematic illustration of a tensile specimen defining strain directions.

3.3.1 Anisotropy/Coherence with previous work?

The anisotropy of the material was determined by Hågensen (2016). To assure that the plates in the present work were heat treated similarly to the plates used in the project work, tensile tests in monotonic loading were performed in the directions RD, RD+30° and RD+90°, with two parallels in each direction. The tensile specimens were cut by the workshop and had measurements as shown in Figure 3.3, which were similar as the measurements of the tensile specimens used by Hågensen (2016). The tensile tests were performed in a Zwick 2.5 kN tensile testing machine with a laser extensometer. The tests were performed to fracture.

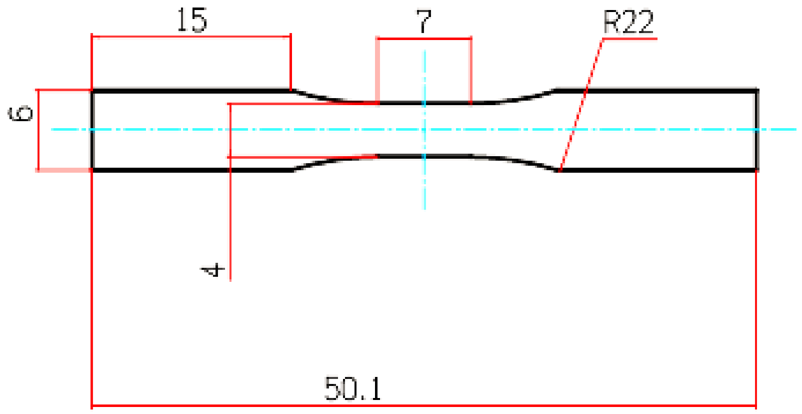

Figure 3.3: Geometrical measurements of specimens used for tensile testing.

3.3.2 Cold rolling

The brass was prestrained by cold rolling in a flat rolling mill, as illustrated in Figure 3.4, at room temperature. The annealed brass plates were first cut to the dimensions $8 \times 10\ cm^2$ to fit the dimensions of the rolling mill. The plates were rolled down to two different thicknesses of 0.96 mm (4% reduction) and 0.92 mm (8% reduction). The plates were rolled in the TD direction. The plates were rolled several times to accurately obtain the desired thicknesses. The plate thicknesses were measures by a digital calliper.

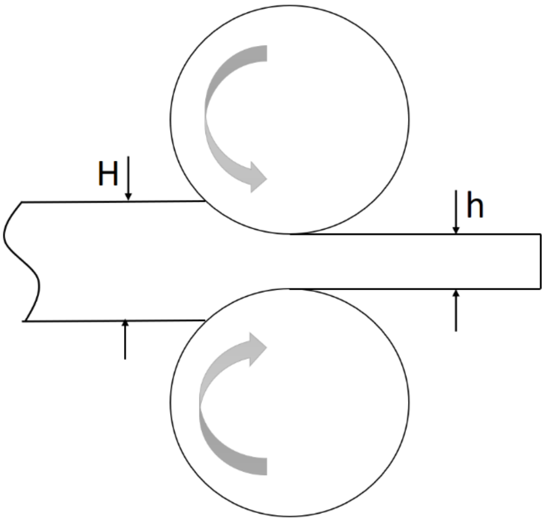

Figure 3.4: Schematic illustration of the experimental setup of flat rolling, where the thickness is reduced from H to h.

3.3.3 Tensile testing

For each of the two prestrain values, tensile specimens were cut in seven different directions between RD and TD, where TD was the direction of prestrain. The global angle between the prestrain and subsequent strain directions are labelled $\beta = (0°, 15°, \dots, 90°)$. There was a necessary time delay of three weeks between rolling and subsequent tensile testing due to the time it took for the workshop to cut tensile specimens from the rolled plates. Three tensile specimens were cut in each series, with the dimensions show in Figure 3.3. The tensile specimens were tested using a Zwick 2.5 kN tensile testing machine with a laser extensometer.

3.3.4 Time delay

The mechanical test done by Hågensen (2016), and in the present work, could not be performed without a minimum time delay between prestrain and subsequent strain. This is due to the time it took to cut new tensile tests from the prestrained specimens, and the fact that different mounts had to be used between compression and tension in the Zwick 2.5 kN tensile testing machine. The time delay between the rolling and tensile testing was about three weeks, the time delay for the two-step tensile testing was about three days, and the time delay between the compression and tensile testing was about 5 minutes.

To investigate the effects of time delay tensile tests were performed with and without time delays. Three monotonic tests were also carried out for reference. To tests were prestrained to 8 %, unloaded, and subsequently strained to fracture after a time delay of about 5 minutes. To tensile tests were prestrained to 8 %, unloaded, and subsequently strained to fracture after a time delay of about three weeks.

4 Results

In the following section, the experimental results are presented, together with calculations used to obtain these results. The material was characterized by grain size, texture and yield locus. The mechanical effects of strain path changes with three different prestrain modes (rolling, tensile and compression) and a variety of prestrain values is presented, together with the respective hardening rates. The mechanical characteristics of the annealed plates used in the present work are compared to the annealed plates used by Hågensen (2016). To investigate the possible effects of time delay between the two strain paths, two-step tensile tests were performed with various time delays.

4.1 Characterization of the initial material

The annealed brass plates were characterized by an EBSD scan in SEM to find the texture and grain size of the initial material. Monotonic tensile tests were performed at different directions relative to RD to measure the anisotropy.

4.1.1 Grain size

Figure 4.1 shows the merged area that was scanned by EBSD, with marks on the detected grain-boundaries. Figure 4.2 shows the grain size distribution obtained by the EBSD scan.

The average grain size was found to be 52.1 µm. Other details about the scanned area is listed in Table 4.

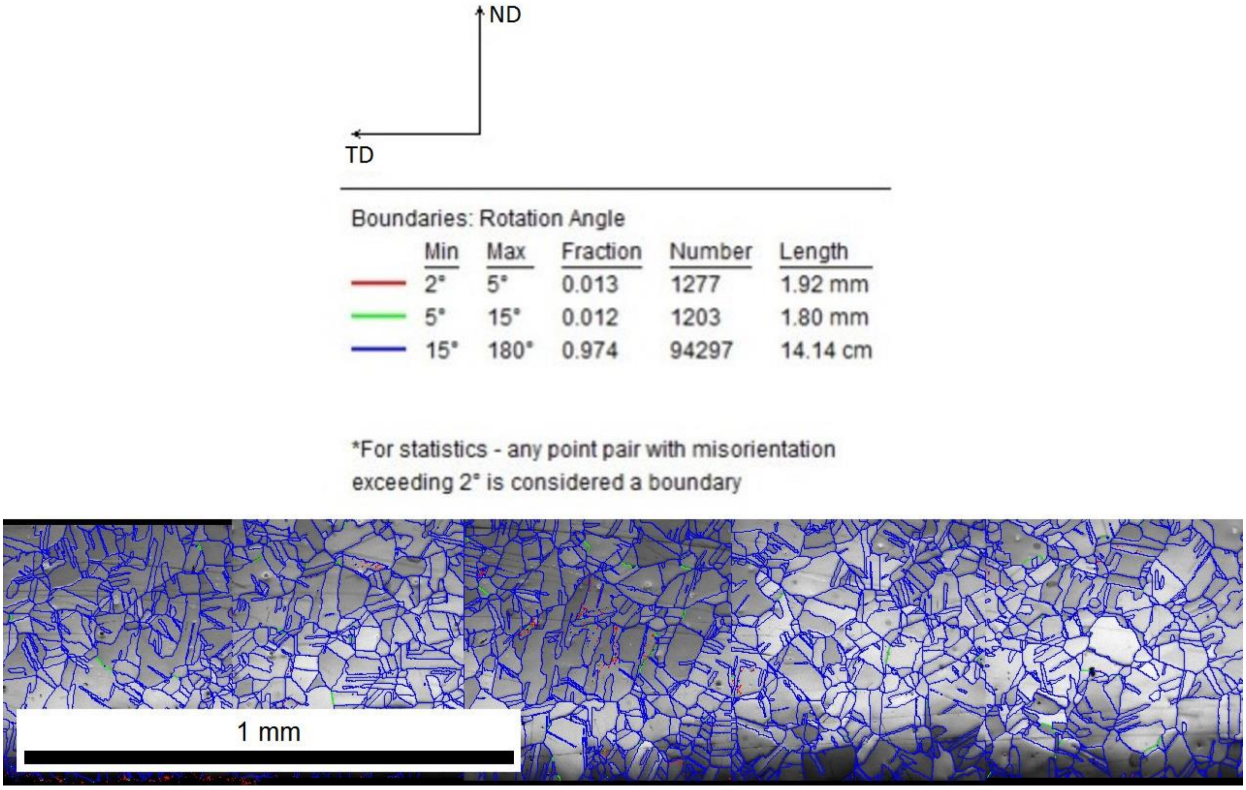

Boundaries: Rotation Angle

	Min	Max	Fraction	Number	Length
🟥	2°	5°	0.013	1277	1.92 mm
🟩	5°	15°	0.012	1203	1.80 mm
🟦	15°	180°	0.974	94297	14.14 cm

*For statistics - any point pair with misorientation exceeding 2° is considered a boundary

Figure 4.1: Image of the scanned area with marked grain boundaries.

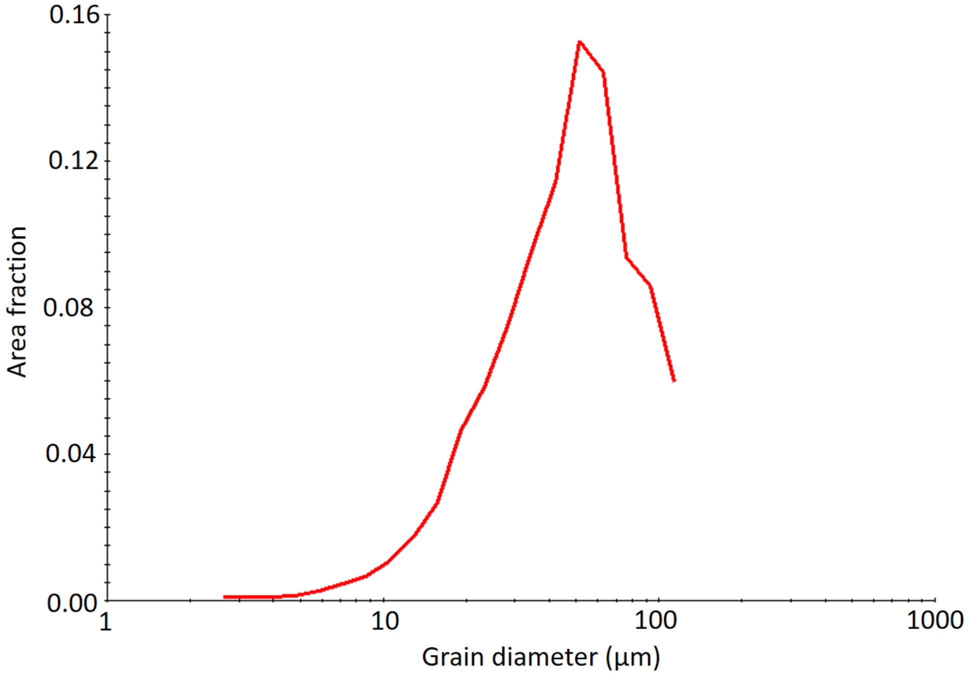

Figure 4.2: Grain size distribution.

Table 4: EBSD scan details.

Number of points in partition	617808
Fraction of points in partition	1.000
Number of indexed points	597133
Average Confidence Index	0.86
Average Image Quality	400700.34
Average Fit [degrees]	0.61
Phases	Copper
Number of grains	2621
Number of edge grains	152

4.1.2 Texture

Figure 4.3 shows an ODF ($\varphi_2 = 0°,\ 5°, \dots, 90°$) of the annealed brass plates prior to any deformation. The observed texture component is similar to that observed by Brickenkamp (1983) for grain growth after annealing of rolled α-brass {197}⟨211⟩.

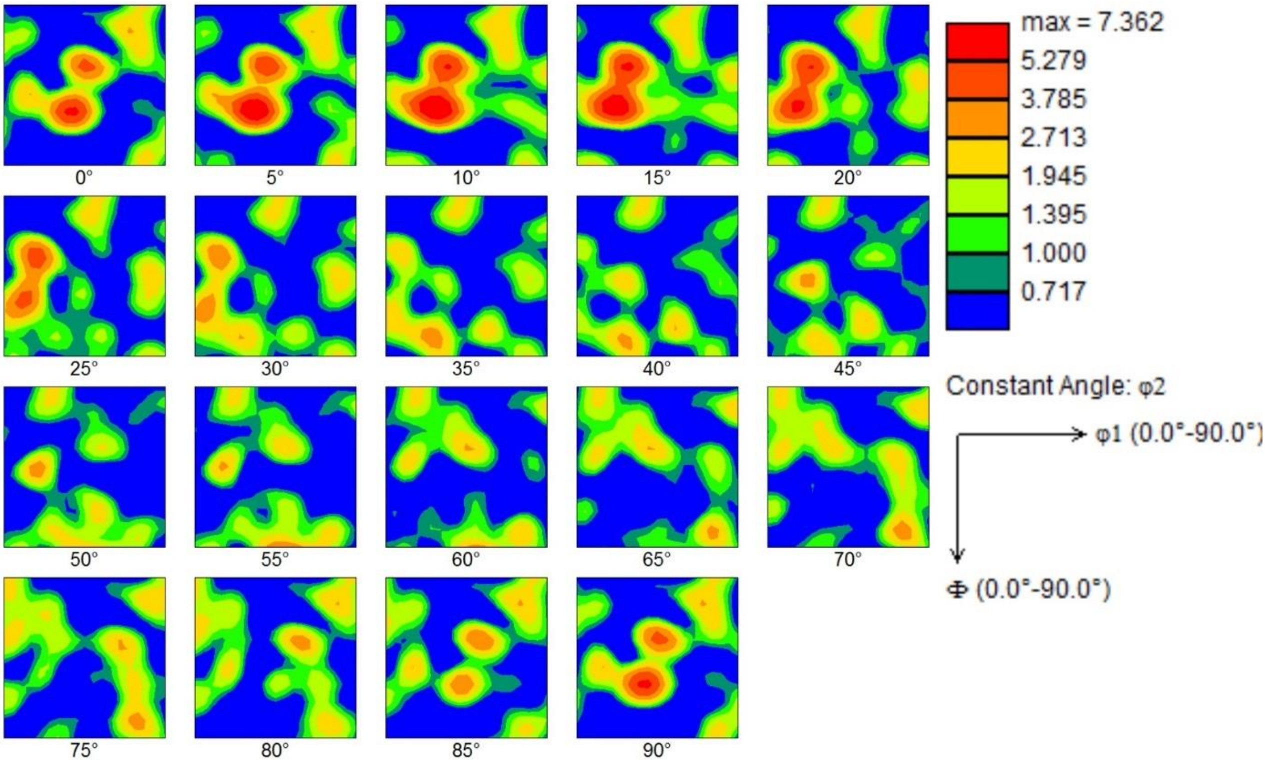

Figure 4.3: ODF ($\varphi_2 = 0°,\ 5°, \dots, 90°$) obtained by EBSD

4.1.3 Yield surface

The annealed brass plates were tested in seven different directions with 15° increments between RD and TD to investigate the anisotropy of the material (Hågensen, 2016). Figure 4.4 shows the true stress strain curves which were used to find the normalized yield stresses and yield locus.

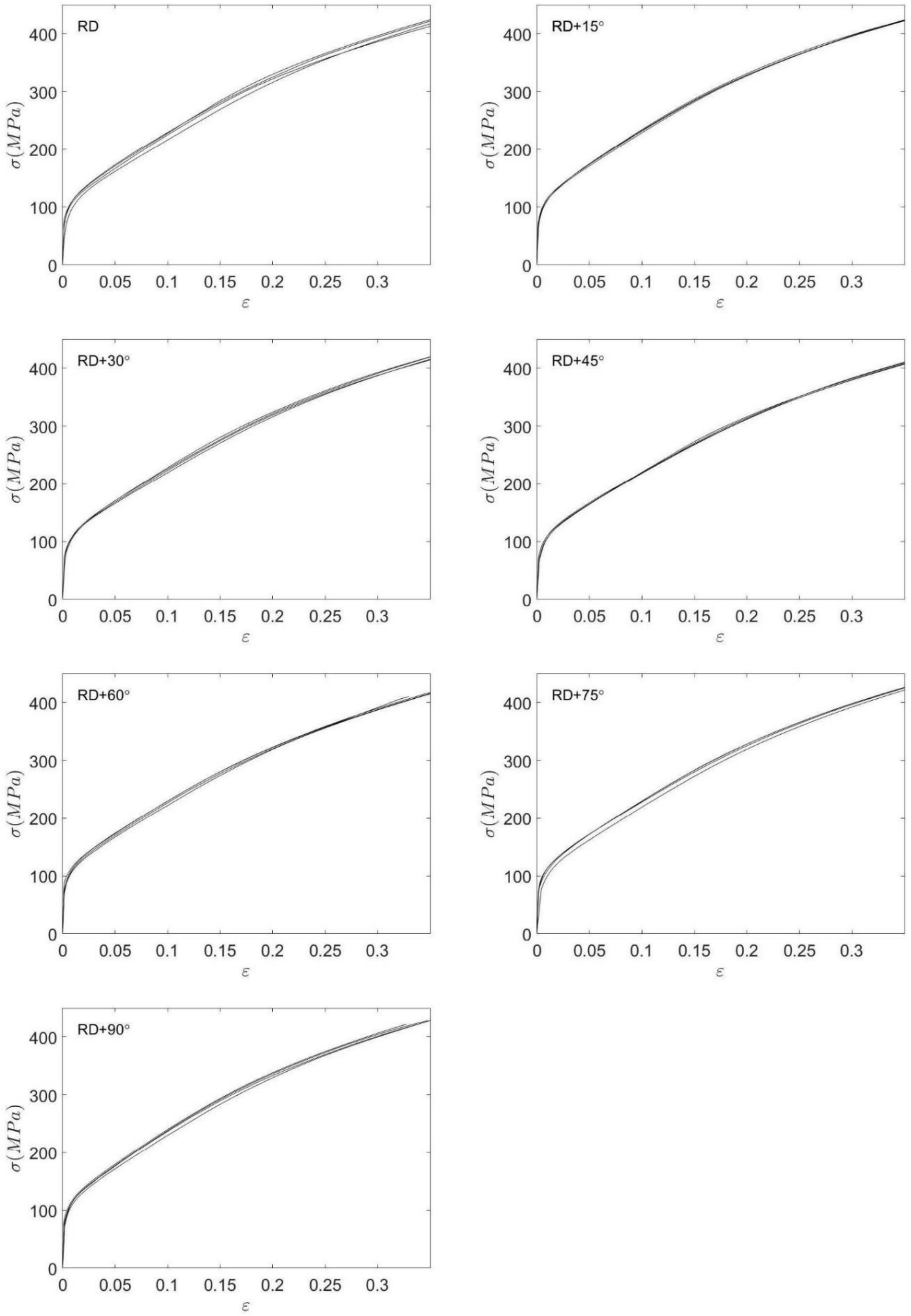

Figure 4.4: *True stress-strain curves for uniaxial tension in seven directions with 15° increments between RD and TD.*

The yield locus was calibrated using the Yld2004-18d model (Barlat et al., 2005) in a MATLAB script by Kai Zhang and Tomas Manik, which is attached in Appendix A. The 3-dimentional surface is identified by 18 parameters, however, in the present work a 2-dimensional yield locus was identified by 16 parameters. The true plastic strain in the loading direction was calculated in MATLAB using work consistence between the graphs in Figure 4.4. The results from these calculations are listed in Table 5.

Table 5: Stress and strain values for monotonic loading in seven directions, for an amount of work of approx. 50 MPa.

α (°)	Work MPa	Strain (-)	Stress (MPa)	Stress ratio (-)	Strain ratio (-)
0 (RD)	50.059026	0.213685	342.968315	1	1
15	50.009172	0.212598	340.727287	0.99346579	0.99491307
30	50.024702	0.217904	335.439314	0.97804753	1.01974402
45	50.030609	0.219837	331.84028	0.96755375	1.02879004
60	50.005092	0.214192	335.996805	0.97967302	1.00237265
75	50.003101	0.213619	341.806196	0.99661158	0.99969113
90 (TD)	50.016714	0.208956	346.017563	1.00889076	0.97786929

The r-values in the seven respective directions were found by Hågensen (2016), by measuring length and width elongation during tensile testing in the seven directions and using equation (16). The r-values are listed in Table 6. Figure 4.5 shows normalized yield stress and r-values, and their trends calibrated by Yld2004-18d, using MATLAB (Appendix B).

Table 6: R-values for the seven directions α between RD and TD. r_1 and r_2 are values measured by two different parallels, and r_{av} is the average of the two.

α (°)	0	15	30	45	60	75	90
r_1	0.904	0.963	1.031	1.143	1.127	1.062	1.046
r_2	0.898	1.026	1.062	1.099	1.075	1.046	1.034
r_{av}	0.901	0.994	1.047	1.121	1.101	1.054	1.040

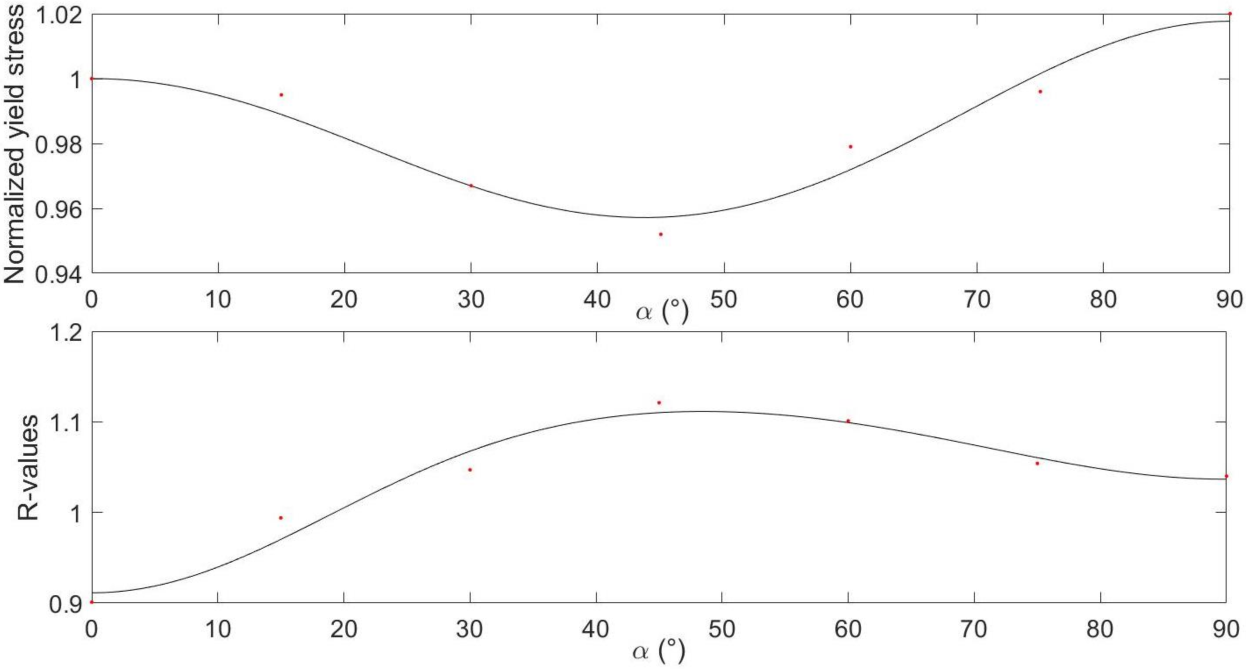

Figure 4.5: Normalized yield stresses and r-values for α = (0°, 15°,…,90°).

The revised ALAMEL model by Zhang et al. (2015) was used for finding the biaxial flow stress and r-value. Texture data from the EBSD scan was used as input in a program by Kai Zhang. Euler angles for the 30 000 positions with highest CI were used for this purpose, and the biaxial values were found to be $r_{bi} = 1.1504$ and $\sigma_{bi} = 1.0281\ MPa$. The resulting yield locus is shown in Figure 4.6.

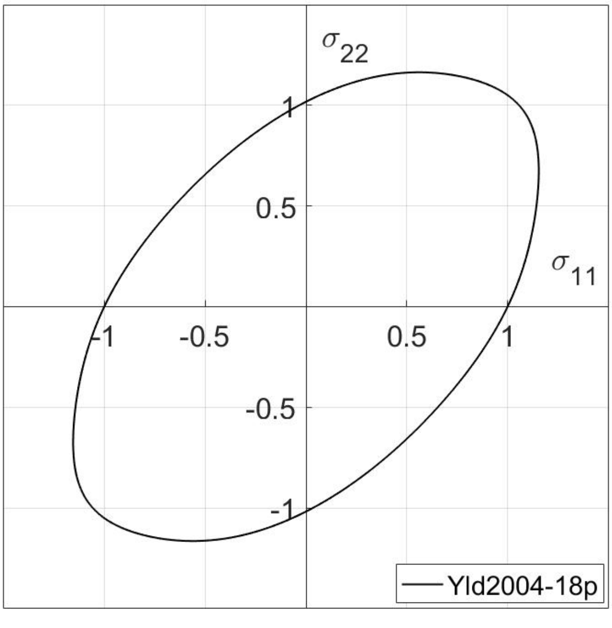

Figure 4.6: The two-dimensional Yld2004-18p locus.

4.2 Mechanical testing

The results from the mechanical testing performed in the present work are presented along with the results from mechanical testing performed by Hågensen (2016).

4.2.1 Uniaxial tensile tests in various plate directions

Nominal stress-strain values from the tensile testing software were converted to true stress-strain values by equations (5) and (6). The graphs were then plotted with the tensile testing results in 0°, 30° and 90° found by Hågensen (2016), to see if the graphs were coherent. The three plots are shown in Figure 4.7.

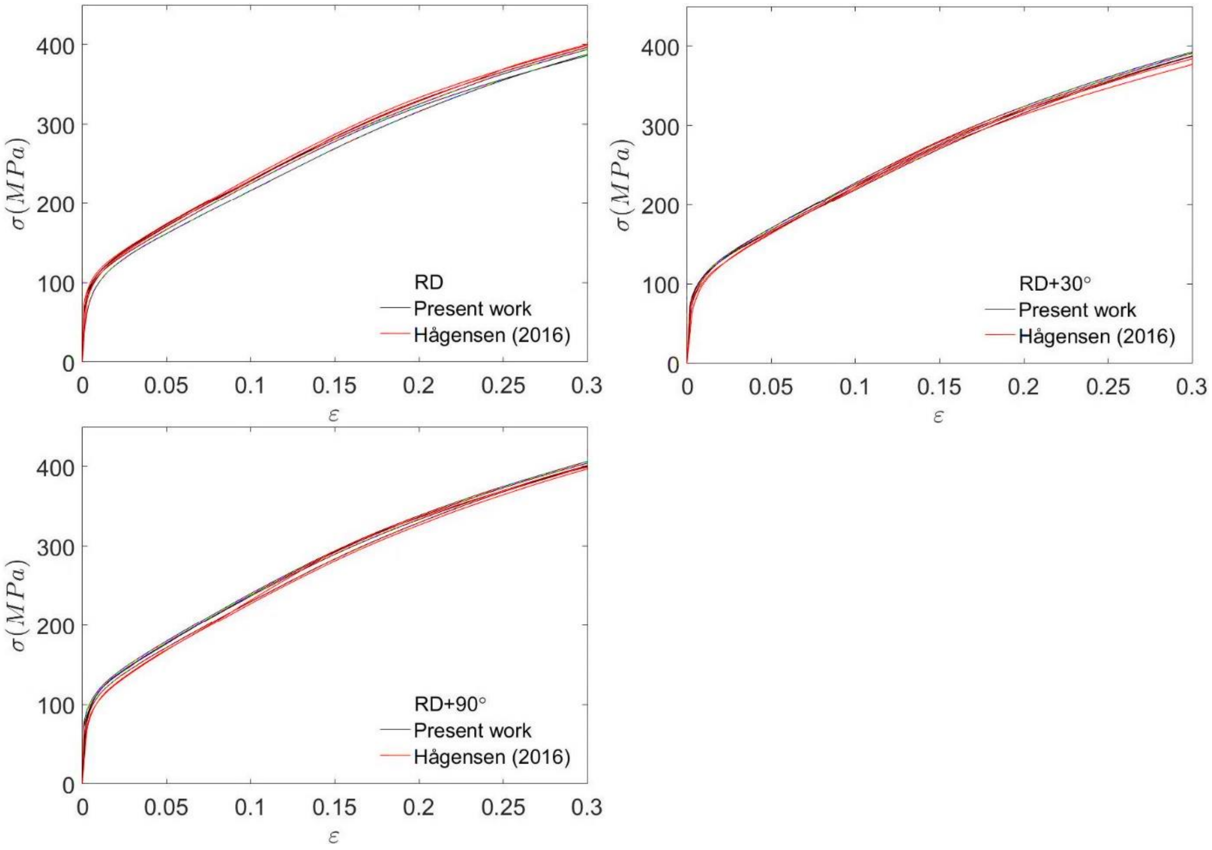

Figure 4.7: Stress-strain curves of uniaxial tensile tests at 0°, 30° and 90° to RD, for plates annealed in the present work, and plates annealed in the work by Hågensen (2016).

4.2.2 Tensile tests with rolling prestrains

Nominal stress-strain values from the tensile testing software were converted to true stress-strain values by equation (5) and (6). The effective prestrain values at the different directions were calculated by the von Mises equivalent strain

$$\bar{\varepsilon} = -\frac{2}{\sqrt{3}}\varepsilon_3 = -\frac{2}{\sqrt{3}}\ln\frac{h}{H}, \tag{23}$$

and are listed in Table 7.

Table 7: Equivalent Von Mises strain values after prestrain by rolling.

Measured thickness reduction	4.0%	8.0%
$\bar{\varepsilon}_{VM}$	4.7%	9.6%

The magnitude of the strain path changes and Schmitt angles were calculated by the equations (17) and (19), respectively, and are listed in Table 8. The R-value for rolling is 0 when rolling a large plate where the plate width is constant. The true stress-strain curves are shown in Figure 4.8, and normalized strain hardening rates are shown in Figure 4.9.

Table 8: Magnitude of strain path change and Schmitt angles for seven straining directions relative to TD.

β (°)	0	15	30	45	60	75	90
θ (°)	30.65	36.89	50.81	65.92	78.18	86.58	88.28
$\cos\theta$	0.8603	0.7998	0.6319	0.4081	0.2049	0.0597	0.0301

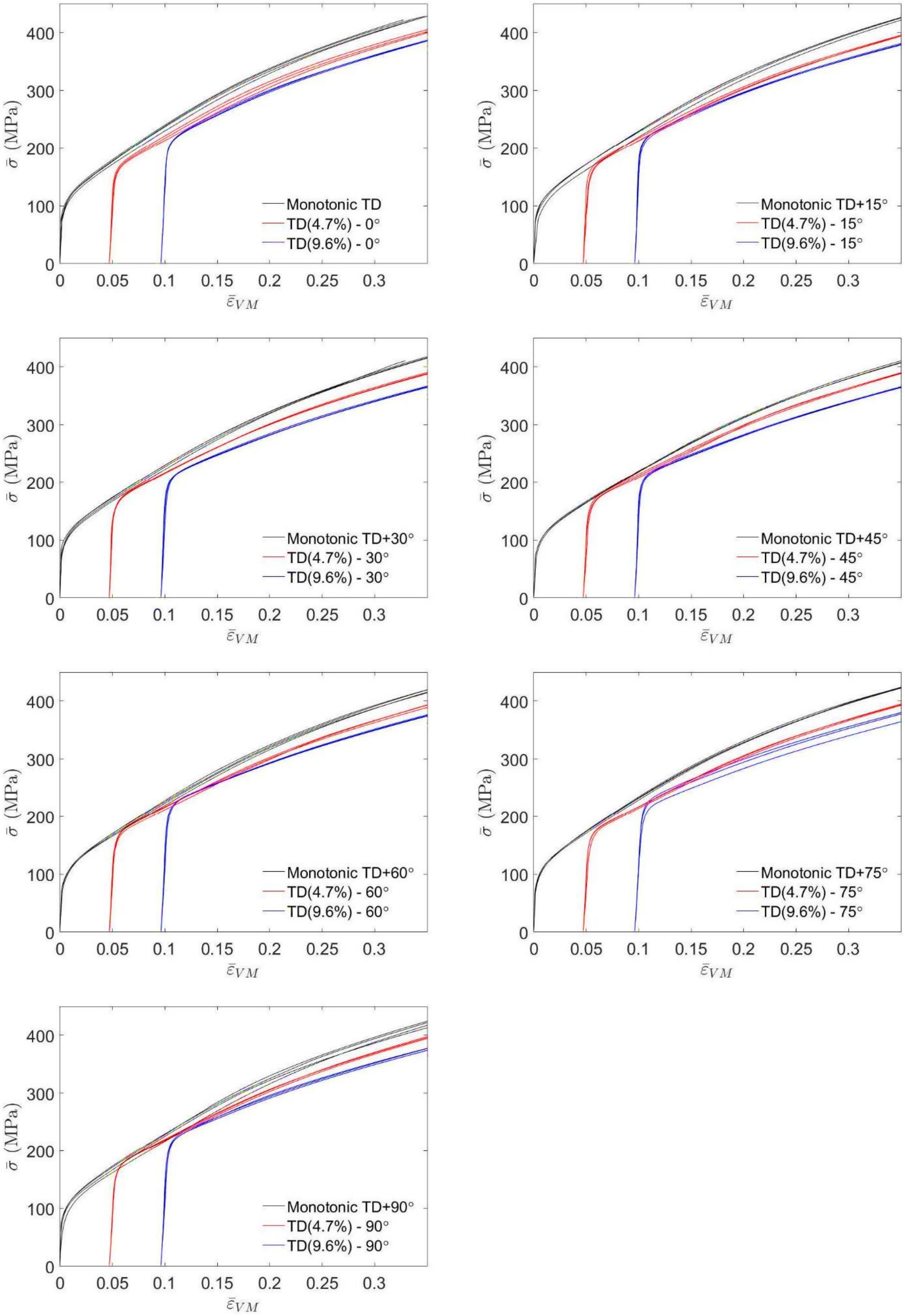

Figure 4.8: Stress-strain curves of tensile test subject to 4.7% and 9.6% prestrain by rolling at β = (0°, 15°,…,90°), and a monotonic loading curves for reference.

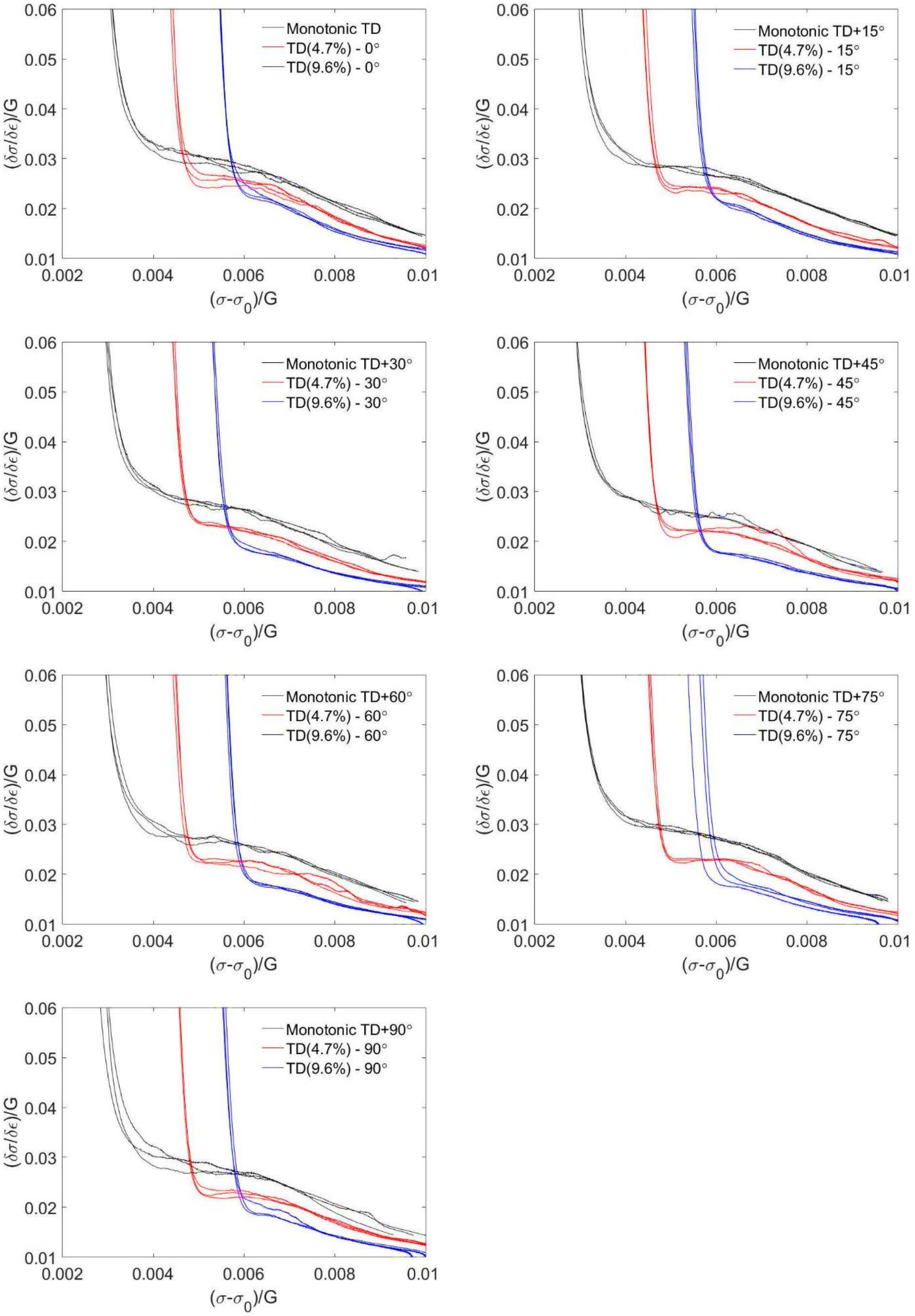

Figure 4.9: Normalized strain hardening rate for monotonic loading and specimens prestrained to 4.7% and 9.6% by rolling, at β = (0°, 15°,…,90°).

The ultimate stress-strain values were found by converting the maximum nominal stress value, and associated strain value, to true stress-strain values. In Table 9, the average ultimate strength values for all loading directions are listed, for monotonic loading and tensile tests prestrained to 4.7% and 9.6% by rolling.

Table 9: Average ultimate strength values for monotonic loading and tensile tests prestrained to 4.7% and 9.6% by rolling.

	ε_u (-)	Deviation of ε_u (%)	σ_u (MPa)	Deviation of σ_u (%)
Monotonic	0.389	-	439.3	-
4.7% prestrain	0.415	+6.68	424.4	−3.51
9.6% prestrain	0.432	+11.05	411.6	−6.73

4.2.3 Tensile tests with tensile prestrains

Calculations of effective prestrains were based on tensile tests in monotonic loading from the work by Hågensen (2016). The work in the RD was set equal to the work at the six other directions, respectively, to find equivalent strain values. This procedure was done in a MATLAB program. The true stress-strain curves are shown in Figure 4.10, and normalized strain hardening rates are shown in Figure 4.11. The magnitudes of strain path change and the Schmitt factors were found by equation (20). The prestrain values, magnitudes of strain path change, and Schmitt angles are listed in Table 10.

Table 10: Properties related to different strain path change angles. ε_p is the level of prestrain, $\cos\theta$ is the magnitude of strain path change, and θ is the Schmitt angle.

α (°)	0	15	30	45	60	75	90
ε_p (%)	7.743	7.76	7.91	7.93	7,70	7,76	7,55
$\cos\theta$	1	0.901	0.628	0.248	-0.124	-0.387	-0.484
θ (°)	0.0	25.7	51.1	75.7	97.2	112.9	119.0

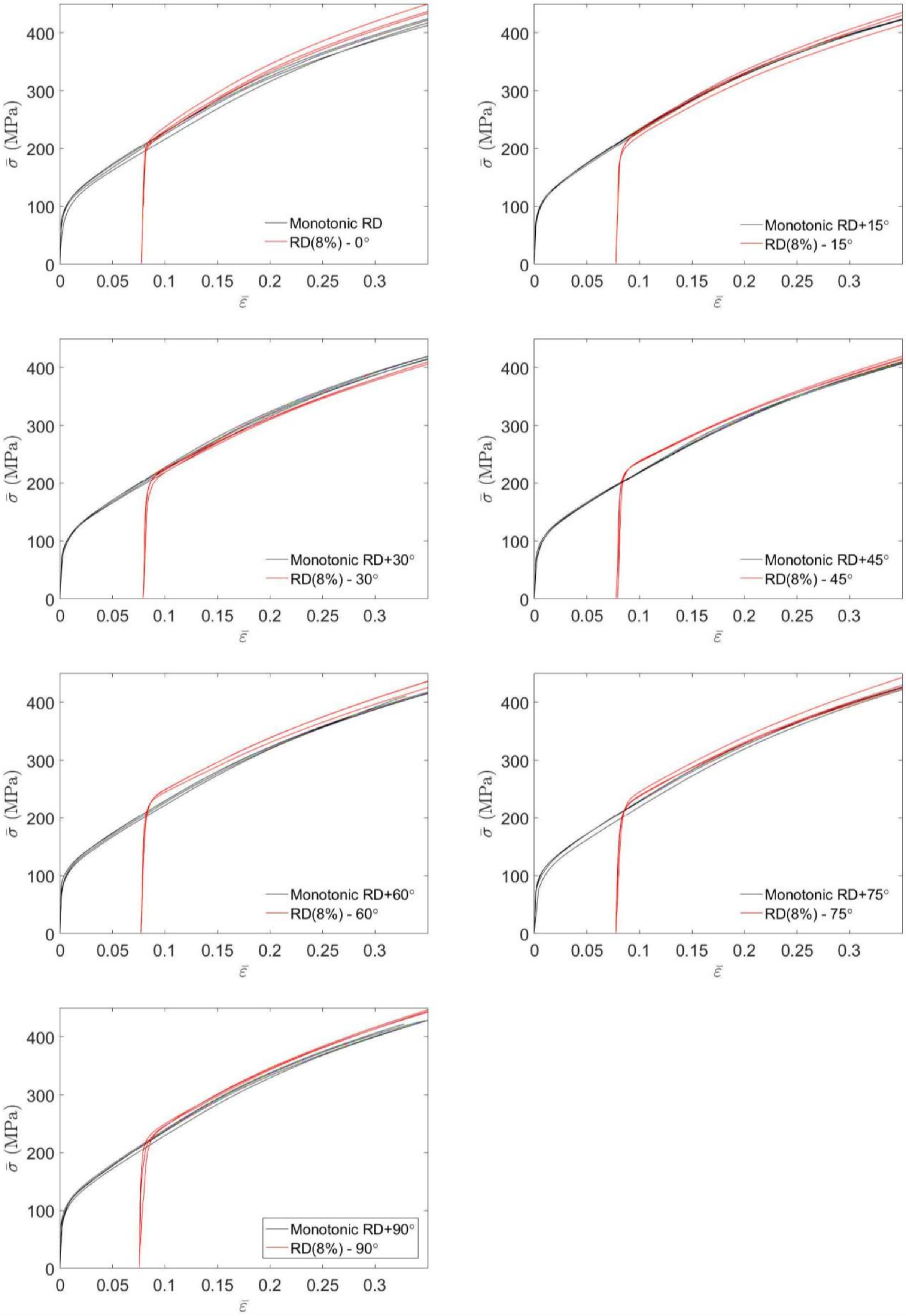

Figure 4.10: The tress-strain curves of monotonic loading and two-step tensile tests with prestrain to 8%, at α = (0°, 15°,…,90°).

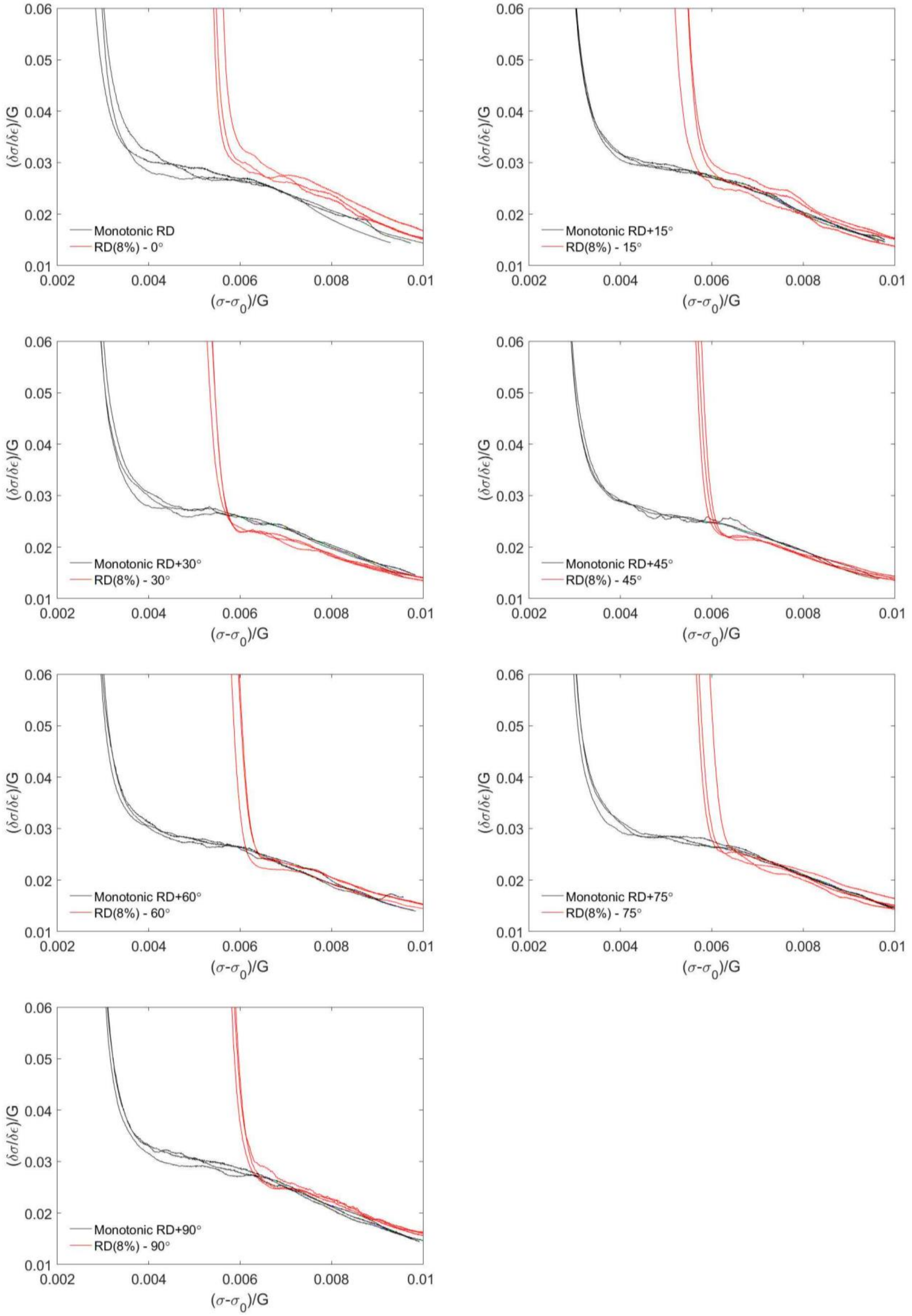

Figure 4.11: Normalized strain hardening rates for two-step tensile tests with 8% prestrain in RD, and subsequent strain in seven different directions between RD and TD. Monotonic hardening curves serve as references.

The ultimate stress-strain values were found by converting the maximum nominal stress value, and associated strain value, to true stress-strain values. In Table 11, the average ultimate strength values for all loading directions are listed, for monotonic loading and tensile tests prestrained to 8% by tensile tension.

Table 11: Average ultimate strength values for monotonic loading and tensile tests prestrained to 8% by tensile.

	ε_u (-)	Deviation of ε_u (%)	σ_u (MPa)	Deviation of σ_u (%)
Monotonic	0.389	-	439.3	-
8% prestrain	0.439	+12.85	475.1	+8.15

4.2.4 Tensile tests with compression prestrains

Figure 4.12 shows the experimental stress-strain curves resulting from tensile tests prestrained to 2% and 4% in compression. The strain hardening curves are shown in Figure 4.13. The Schmitt angle for reverse strain path change was found by equation (18), using $r_2 = r_1$ and $\alpha = 180°$, and was found to have a value of $\theta = 0°$ ($\cos\theta = 1$).

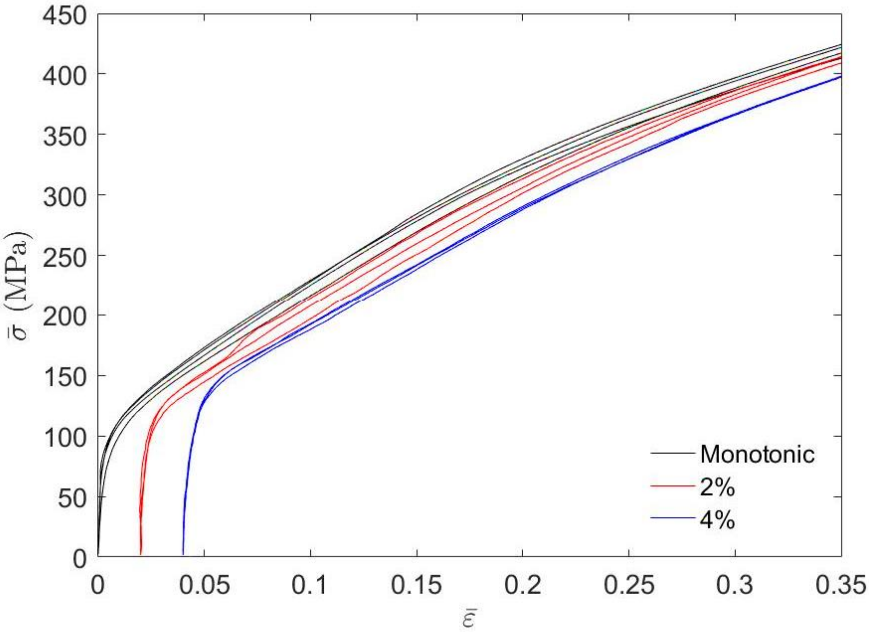

Figure 4.12: Stress-strain curves for low brass strained in the RD subsequent to 2% and 4% prestrain by compression, and monotonic loading curves as reference.

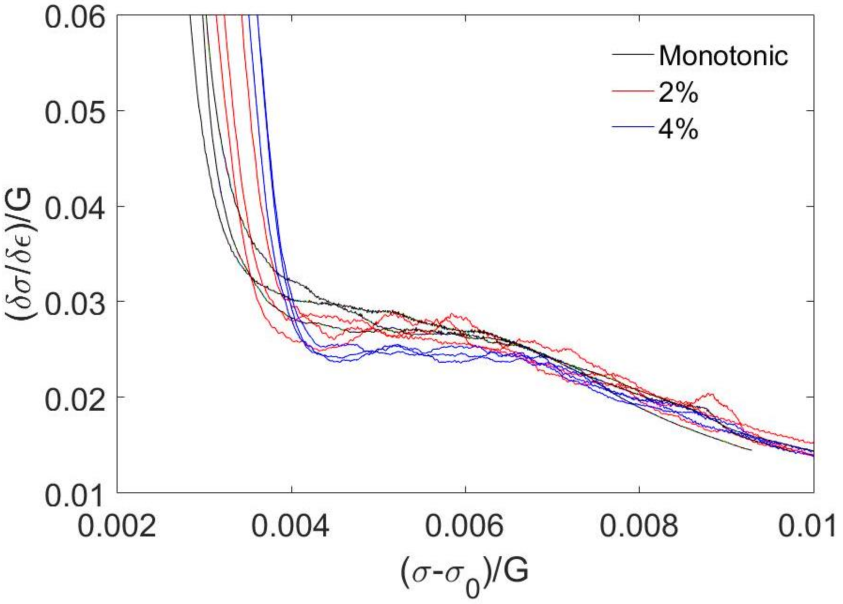

Figure 4.13: Normalized strain hardening rate for specimens prestrained to 2% and 4% by tensile compression. Monotonic curve serves as reference.

The ultimate stress-strain values were found by converting the maximum nominal stress value, and associated strain values, to true stress-strain values. In Table 12, the average ultimate strength values for all loading directions are listed, for monotonic loading and tensile tests prestrained to 2% and 4% by compression.

Table 12: Average ultimate strength values for monotonic loading and tensile tests prestrained to 2% and 4% by compression.

	ε_u (-)	Deviation of ε_u (%)	σ_u (MPa)	Deviation of σ_u (%)
Monotonic	0.389	-	439.3	-
2% prestrain	0.463	+19.0	469.9	+7.0
4% prestrain	0.442	+13.6	445.4	+1.4

4.2.5 Time delay

Figure 4.14 shows the stress-strain curves with and without time delays after 8% prestrain by tensile in tension. The nominal stress-strain curves were converted to true stress-strain curves by equations (5) and (6).

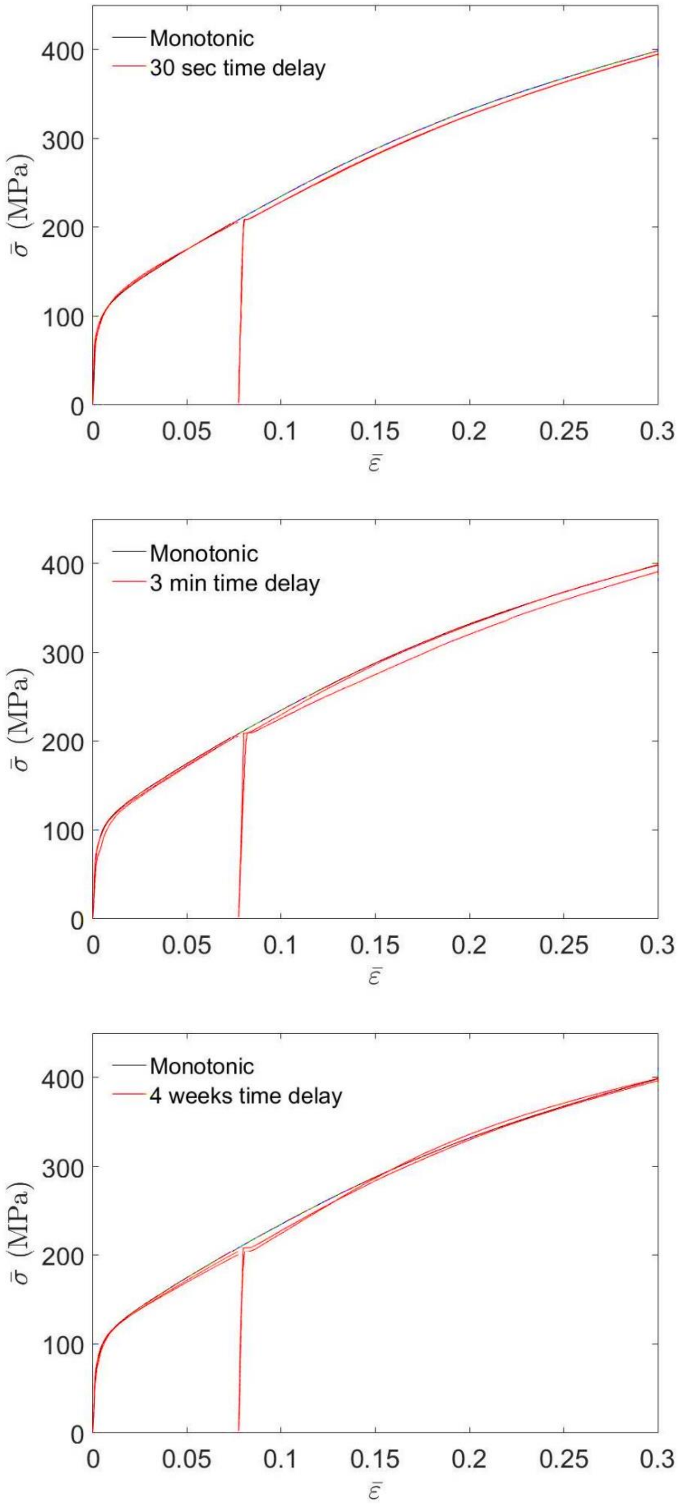

Figure 4.14: Stress-strain curves of monotonic loading in RD, and two-step tensile tests with 8% prestrain and various time delays (30 sec, 3 min and 4 weeks) between the two strains.

5 Discussion

The following section discusses the experimental results obtained in the present work, and the work by Hågensen (2016), as well as some possible microstructural mechanisms leading to the observed effects. The accuracy of the mechanical testing and calculations are also considered.

5.1 State of the initial material

The low brass was annealed for 5 hours and 10 minutes at 600°. According to the annealing curve for this material, this should be sufficient for total recrystallization (Hågensen, 2016). The SEM imaging of the metal also resembles that of a recrystallized metal, with apparent annealing twins (Figure 4.1). The average grain size was found to be 52.1μm, when including the twin boundaries, which indicates that the grains have grown substantially after recrystallization. The EBSD scan was performed with a CI value of 0.86, indicating high confidence in the orientation indexing. The ODF (Figure 4.3) shows a weak texture with a maximum ODF intensity of 7.362. There is one apparent texture component $\{197\}\langle 211\rangle$, which have been identified for similar α-brass in previous studies (Gottstein and Shvindlerman, 2009). Monotonic uniaxial tensile tests at seven directions relative to RD reviled a slight anisotropy in the material. The brass was strongest in RD and TD, and weakest in RD+45°.

5.2 Tensile tests with rolling prestrain

The specimens that were prestrained by rolling all showed reduced reloading yield strengths compared to the monotonic curves, i.e. the Bauschinger effect. This result is consistent with result found for Cu-30%Zn prestrained by rolling (Sakharova et al., 2009, Sakharova et al., 2008). Some of the specimens prestrained to 4.6% had an initial yield strengths equal to the reference curve before the strength was reduced. Some of the specimens prestrained to 9.6% had an initial yield strength equal to the specimens prestrained to 4.6%. The stress curves did not behave as the monotonic curves, but had reduced strain hardening rates after reloading. The magnitude of the response was greater for a larger prestrain value of $\bar{\varepsilon} = 4.7\%$, than for $\bar{\varepsilon} = 9.6\%$, which is consistent with the reduced strain hardening rate. The magnitude of the path change could not be easily distinguished for the various Schmitt values, and the Schmitt values only ranged from 30.65° to 88.28°. For the specimens prestrained by 2% and 4%, the ultimate stress was reduced by 3.51% and 6.73%, respectively. The ultimate strain increased by 6.68% and 11.05%.

5.3 Tensile tests with tensile prestrain

The two-step tensile tests induced an increased reloading yield strength for most of the angles α. Only $\alpha = 0°, 15°$ and $30°$ has reloading curves that coincide with the monotonic curves. The overshoot was permanent, only a slight decrease in the overshoot with larger strain levels was observed for some curves. There was also some spread among the curves for some directions, especially $\alpha = 0°, 60°$ and $75°$, which made it difficult to determine whether the hardening rates were increasing or decreasing. Figure 5.1 shows the stress-strain for the curve with $\alpha = 45°$ and $60°$, which showed the permanent increase in yield strength most clearly. These were also the most orthogonal strain-path changes ($\cos\theta$ closest to 0). The yield strengths did not increase at the expense of the ultimate strength, which increased by 12.85%, and ultimate strain increasing by 8.15%, on average for all curves. To the knowledge of the author, this effect of strain-path change has not previously been published in the literature.

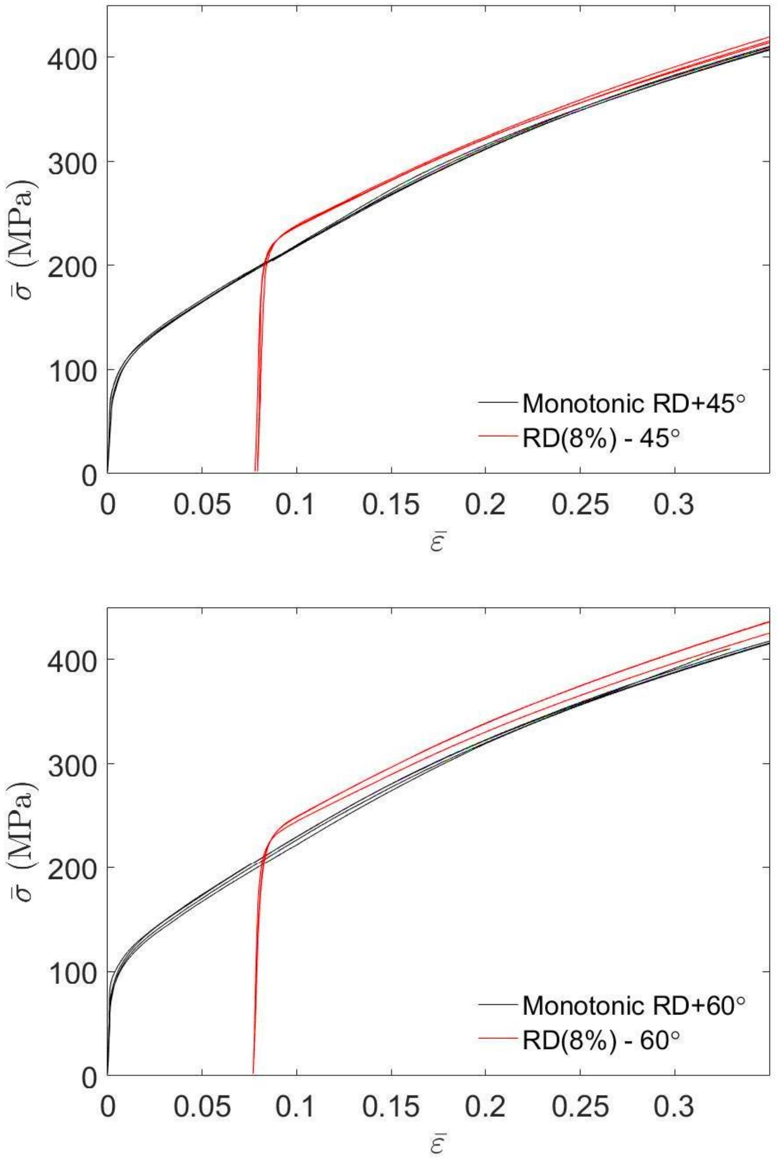

Figure 5.1: Stress-strain curves for specimens prestrained to 8% in RD+45° and RD+60° directions, and monotonic curves as references.

5.4 Tensile tests with compression prestrain

The specimens prestrained by compression in tension showed permanent reduction of the yield stress, i.e. the Bauschinger effect. The prestrained curves behaved similarly to the reference curve, only at lower stress levels. The magnitude of the response was greater for a larger prestrain value of $\bar{\varepsilon} = 2.0\%$, than for $\bar{\varepsilon} = 4.0\%$. For reverse strain-path change $\cos\theta = -1$, and $\theta = 180°$. The ultimate strength of the specimens prestrained by compression to 2% and 4% increased compared to that of monotonic loading, by 7.0% and 1.4% respectively (Table 12). This can also be seen in Figure 5.2, where the true stress strain is plotted to the points of ultimate strength.

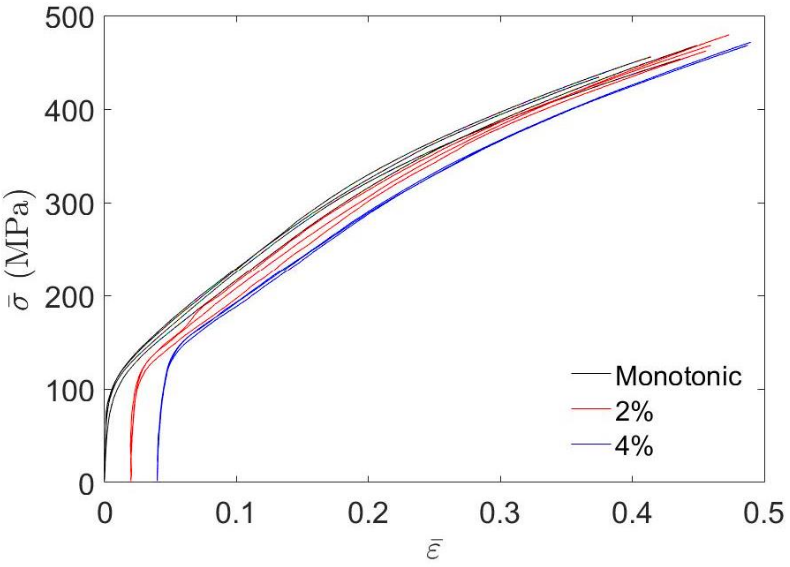

Figure 5.2: Stress-strain curves of monotonic loading in RD and specimens prestrained to 4.T% and 9.6% by compression in tension.

5.5 Comparing loading modes

The modes of preloading had a significant impact on the resulting mechanical effects. The two-step tensile tests had an increased hardening response, while rolling and compression prestrain resulted in a Bauschinger response. The Bauschinger effect was greater for specimens prestrained by compression, however, prestrain by rolling showed a reduced strain hardening rate. Corrêa et al. (2002) investigated the effects of strain path changes by tension and torsion, for Cu-30Zn. It was found that the behaviour after reloading was dependent on the tension/torsion sequence, which lead to opposite behaviours, and prestrain magnitude. The significance of loading modes can be related to the present findings.

For all preloading modes, the mechanical effect of strain-path changes was permanent, the behaviour did not go back to its original behaviour. Corrêa et al. (2002) found that strain path changes in Cu-30Zn was more permanent than strain path changes in low carbon steel, which is in accordance with the present observations. Another similarity between prestraining modes is that the ultimate strength was not reduced because of instabilities, which have been reported to follow strain-path changes for some metals like steel and aluminium (Li and Bate, 1991, Rauch and Schmitt, 1989). This could mean that the mechanisms for the three path changes in the present work are somewhat consistent.

5.6 Sources of behaviour

Cu-20Zn is a low SFE metal that typically will deform by twinning in addition do dislocation movement. Plots of the work-hardening rate versus stress has been reported to have four stages for low SFE metals such as low brass (El-Danaf et al., 2000, Asgari et al., 1997, Feaugas, 1999). All strain-hardening plots of Cu-20Zn in the present work shows such a behaviour. For low SFE metals the hardening rate in stage A is typically high. The low SFE hinders the dynamic recovery process since a higher stress is needed to combine partial dislocations and facilitate cross-slip (Salem et al., 2003). From the hardening rate plots, one can see a clear stage B, which is associated with primary twinning. Stage C is also clearly seen in the plots, and this stage has been found to correlate with the decrease in twin formation (Asgari et al., 1997). Stage D of constant strain-hardening was not so pronounced in the strain-hardening plots. This stage is associated with production of secondary twins, which was non-coplanar with the primary slip system. Stage C gradually flattens and hence no clear onset of this mechanism can be found from the plots. Stage D is typically larger than IV hardening rates for medium-to-high SFE metals (McQueen et al., 2016, Argon and Haasen, 1993).

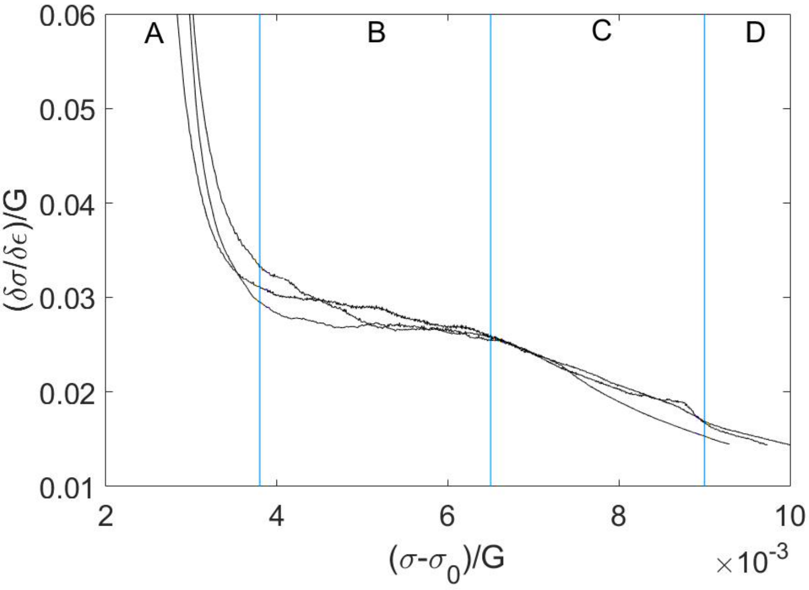

Figure 5.3: Normalized strain hardening response for Cu-20Zn in uniaxial loading.

The mechanical effects of deformation twinning can be explained by the three following mechanisms (Kalidindi et al., 2003); 1) Formation of grain boundary like interfaces that serve as sites for dislocation pile-ups and hence reduce the free slip length. This can be compared to the Hall-Patch hardening mechanism. This is believed to be the dominant strain hardening mechanism exhibited by low SFE metals (Asgari et al., 1997). 2) Activation of new slip systems due to change in the crystal orientation. The formation of twins has a profound influence on the hardening of non-coplanar slip systems, but does not affect co-planar slip systems as much. 3) The formation of glissile dislocations to sessile (Basinski et al., 1997). The net effect of deformation twinning is a higher work hardening rate.

To the knowledge of the author, not many studies are done for strain-path changes in Cu-20Zn, in comparison to Cu-30Zn which is more widely investigated. The increased zinc content in Cu-30Zn decreases the SFE, and this material is generally stronger than Cu-20Zn. Mechanical twins are observed to form faster for higher solute Cu-Zn alloys (Hirsch and Lücke, 1988a, Hirsch and Lücke, 1988b). Venables (1964) suggested that there was a parabolic relationship between the SFE and the stress required for nucleation of deformation twins. This study did however not account for the different solid solution strengthening contributions in the investigated alloys. El-Danaf et al. (1999) suggested that smaller SFE is rather an indirect cause of increased strain hardening. Asgari et al. (1997) suggested a criterion, stated in equation (22), for a critical dislocation density needed for twin initiation. This proposal was underlined by the fact that FCC metals with very different SFE values had twin initiation at nearby the same values of $(\sigma_{tw} - \sigma_0)/G$. El-Danaf et al. (1999) found that stage B initiated when approaching a $(\sigma_{tw} - \sigma_0)/G$ value of 0.003, for 30 to 40 μm grain-sized metals. Figure 5.4 shows that a similar result was observed for the Cu-20Zn with a grain size at about 50 μm.

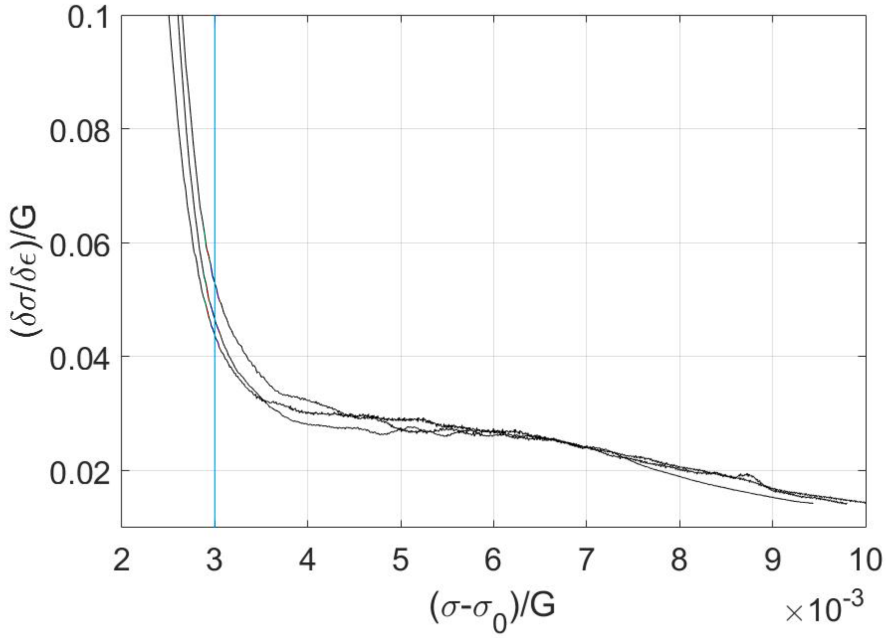

Figure 5.4: Normalized strain hardening response for uniaxial monotonic loading curves in RD.

The extent to which deformation by dislocation glide or twinning are active is directly related to the strain rate, deformation mode, temperature, and initial grain size (Barrett and Massalski, 1980). The strain rate was constant at 1mm/min for all tensile testing, except prestraining by tensile, which were tested at 4 mm/min, since the geometry of the testing area was larger. The effect of strain rate should thus only be used to compare these results with those from other studies. The initial grain size in the present work was found to by 52.1µm, when including the twin boundaries, which indicates that the grains have grown substantially after recrystallization. It has been reported that an increase in the average grain size lowers the twin nucleation stress (Romhanji et al., 1992, Lahaie et al., 1992, Song and Gray, 1995, Somekawa and Mukai, 2013). El-Danaf et al. (1999) found that the grain size has a much greater influence on low SFE metals than on medium SFE metals. The study shows that for a given amount of strain, more deformation twins are formed in large grains than in small grains. This is reflected in the strain hardening rate graphs, which have decreasing distinctions between stage B and C.

The formation of dislocation structures is another deformation mechanism to consider in addition to deformation twinning. For pure copper, and other medium-to-high SFE metals, structural development are observed (Li and Bate, 1991, Rauch and Schmitt, 1989). Structures are unstable following a path change. Destruction of the structure result in a transient lowering of the strain hardening rate. Low SFE metals are less susceptible to this transient reductions than medium-to-high SFE metals (Zandrahimi et al., 1989), which is probably related to the fact that low SFE metals deform by twinning in addition to dislocation slip. The formation of dislocation structures is sensitive to the applied loading mode, and this sensibility increases with applied deformation (Franciosi et al., 1987, Korbel and Martin, 1988). The formation of dislocation structures would assumedly not contribute as much to the observed behaviours for Cu-20Zn as for medium-to-high SFE metals, especially since extensive twinning are apparent from the strain-hardening plots.

During reverse loading the Bauschinger effect is observed. From the hardening rate curves for two-step tensile testing (Figure 4.10), it looks as primary twins are already substantially developed during prestrain. It would have been enlightening to see the stress-train curves and hardening rates for compression and rolling prestraining, however, these were not possible to obtain with the experimental equipment used for this work.

The Bauschinger effect is traditionally explained by internal back stresses at dislocation structures, which support load reversal (Orowan, 1959). Some has also argued that the Bauschinger effects are driven by dislocation concentrations, rather than cell formation (Rauch, 1997). In addition to these effects it was suggested that untangling of dislocation structures upon load reversal releases mobile dislocations, and hence the requirement to activate new dislocation sources is reduced (Rauch and Schmitt, 1989). Some have found that de-twinning is preferred over creating new twins inside the existing twins upon reversal (Proust et al., 2010). This can also contribute to a lower yield stress upon reversal.

The instability and reduced work hardening typically following path change of metals with medium-to-high SFE can also be enhanced by the development of shear bands or other heterogeneous formations (Li and Bate, 1991). These instabilities can lead to premature fracture and reduced ultimate strain. Such effects are not observed for the Cu-20Zn tested in the present work. On the contrary, the ultimate strain generally increases after path change (Figure 5.5). The ultimate strength is increased for tensile tests with tensile prestrain, and reduced for the other modes of prestrain (Figure 5.6).

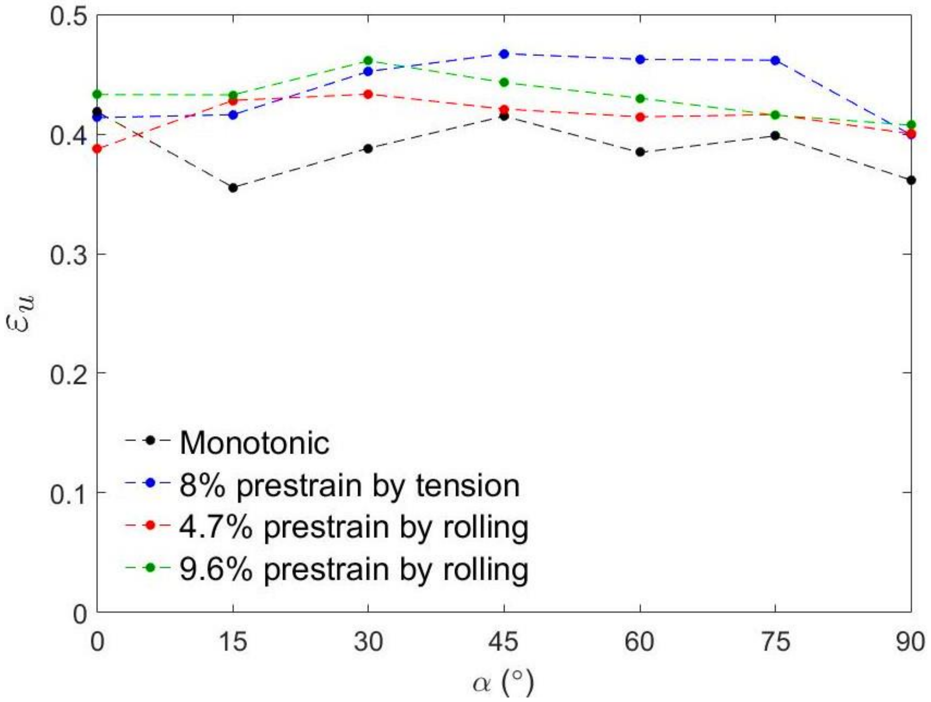

Figure 5.5: Evolution of ultimate strain for various angles and different prestrain loading modes.

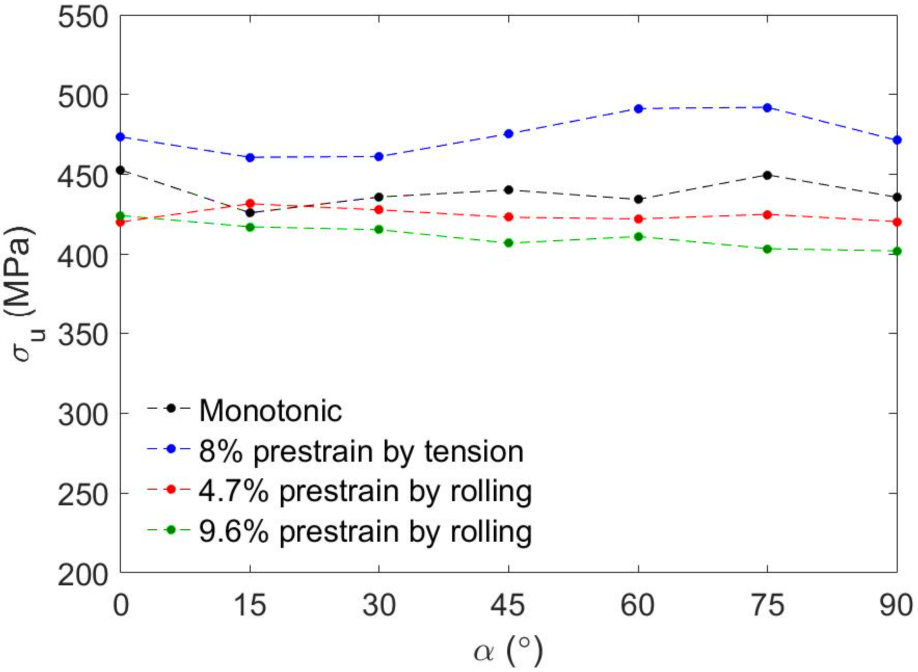

Figure 5.6: Evolution of ultimate strength for different loading modes of prestrain, and at various path change angles.

The above section discusses the microstructural mechanisms operating during strain-path changes for the Cu-20Zn plates are merely speculations. To get a clearer understanding of these mechanisms it would be necessary to do characterization of the metal after prestraining, and also after some subsequent strain. It would be interesting to investigate the formation of dislocation cells and twinning after the various loading modes.

5.7 Result accuracy

The consistency of the annealing process between the brass plates in the present work and the plates in the work by Hågensen (2016) was tested. The brass plates were all annealed for 5 hours and 10 minutes at 600°. Figure 4.7 shows the uniaxial tension curves of the two annealing procedures for three directions, 0°, 30° and 90° to RD. The curves were mostly coinciding in the respective directions, only some curves did not follow the rest for some parts of the strain interval. It is thus no reason to separate the material tested in the present work and the material tested by Hågensen (2016).

Among the presented sets of stress-strain plots some curves showed some degree of scattering, which in some cases made it difficult to determine the trends or relative values of the graphs. This is especially true for the two-step tensile tests. The two-step tensile tests in the RD lies slightly above the reference curves but all curves are scattered which makes it difficult to assess their relative relationships.

As mentioned above the two-step tensile tests in RD do not coincide perfectly. This could possibly be due to the time delay of three weeks between the two loadings, which was necessary for cutting new specimens from the prestrained specimens. Tests were done with various time delays of 30 seconds, 3 minutes and 4 weeks in uniaxial tension in RD, and compared with the monotonic curves. None of the curves showed any significant effects of the time delays as they all coincided with the monotonic curves. The only difference between the two experiments was the geometry of the tested specimens, and the fact that the second samples were cut from the preloaded specimens, by the workshop. It has also been found that the transient response in steel from path change is not a result of strain aging (Doucet and Wagoner, 1987). Another possibility is that unloading the material lead to changes in the microstructure which lead to an increased reloading yield stress. A third explanation could be the low number of tests in each series simply lead to scattering favouring the observed behaviour, but the scattering could also have made the curves coincide. However, there could possibly be other explanations to this observation.

The equivalent strain values were calculated in different ways due to the natures of the different loading modes, and the ability to measure the prestrain values. The prestrain values for the two-step tensile tests were calculated by finding the equivalent stress-strain values for a given amount of work in every direction. The monotonic uniaxial tension curves were used for this purpose, and because several specimens were tested in every direction one reference curve was chosen for each. In addition to this, the work calculations were done numerically in MATLAB, which lead to some inaccuracy.

The equivalent plastic strain in the final loading directions have been calculated in several ways for each of the preloading modes, because of the nature of the loading modes. The calculated equivalent plastic strain depends on the model used and the associated calibration parameters. Using a different model for calculating these strain values could possibly shift the reloading curves some percent.

The prestrains by tension have been converted to the true plastic strain in the final loading direction by work consistence (Barlat et al., 2005). This is an accurate method, however, it is only possible to use when stress-strain curves are available. The prestrains by rolling were identified by the Von Mises equivalent plastic strain (Mises, 1913), using equation (22). This method assumes an isotropic material and would not give the same accuracy as using work consistence. The prestrain values could also have been calculated numerically using the yield locus found for the specific material. This method would give a more accurate result than Von Mises equivalent strain, but it would be difficult to obtain the stress components for the rolling. In addition to the calculation method, the digital calliper used to measure thickness reduction after rolling could contribute to some inaccuracy. The calliper had a resolution of 0.01mm, which could possibly change the 8.8% at a maximum. This would entail an insignificant shift in the curves, which would not have an effect of the observed behaviours. The prestrain values for the specimens prestrained by compression were found by using the strain values measured by the tensile testing machine. These values were used for simplicity, as changing these prestrain values would not shift the curves more than a few percent, and the observable behaviours would be the same.

6 Conclusions

The mechanical effects of strain-path changes in Cu-20Zn plates were investigated in the present work. The brass plates were prestrained by three different loading modes; tensile, compression and rolling. Tensile prestrain was performed to 8%, compression to 2% and 4%, and rolling to 4% and 9%. The obtained results could be summarized as follows:

- Tensile tests prestrained by rolling had a permanent Bauschinger effect, and reduced work hardening. The effect was larger for larger amounts of prestrain.
- Tensile tests prestrained by compression showed a permanent Bauschinger effect, with no change in the work hardening rate. The yield strengths were reduced more for larger amounts of prestrain.
- Tensile tests prestrained by tensile in tension showed a permanent increased work hardening effect. This effect was most evident for $\cos\theta$ values closest to 0.
- The loading mode for prestraining was critical for the observed effects of strain-path changes.
- The ultimate strengths were only slightly reduced for tensile tests prestrained by rolling and compression. Ultimate strains were slightly increased for all modes and amounts of prestrain.
- All tensile tests showed characteristic four-stage strain hardening responses, indicating primary and secondary deformation twinning (stage B and D).

7 Further work

Further investigations are needed in order to assess the mechanical behaviour of Cu-20Zn in greater detail, and get a better understanding of the associated microstructural mechanisms. The following is suggested:

- Two-step tensile tests with more values of prestrain, especially larger prestrains.
- Two-step tensile tests with varying initial grain sizes.
- Testing more strain-rates values. This with particular interest of the amount of deformation twinning after prestrain.
- Microstructural investigations in TEM after prestrain, and after some amount of subsequent strain, to investigate the formation of dislocation structures and deformation twins.

8 References

ARGON, A. S. & HAASEN, P. 1993. A new mechanism of work hardening in the late stages of large strain plastic flow in F.C.C. and diamond cubic crystals. *Acta Metallurgica et Materialia,* 41**,** 3289-3306.

ASGARI, S., EL-DANAF, E., KALIDINDI, S. & DOHERTY, R. 1997. Strain hardening regimes and microstructural evolution during large strain compression of low stacking fault energy fcc alloys that form deformation twins. *Metallurgical and Materials Transactions A,* 28**,** 1781-1795.

BARLAT, F., ARETZ, H., YOON, J. W., KARABIN, M. E., BREM, J. C. & DICK, R. E. 2005. Linear transfomation-based anisotropic yield functions. *International Journal of Plasticity,* 21**,** 1009-1039.

BARLAT, F., BREM, J. C., YOON, J. W., CHUNG, K., DICK, R. E., LEGE, D. J., POURBOGHRAT, F., CHOI, S. H. & CHU, E. 2003a. Plane stress yield function for aluminum alloy sheets—part 1: theory. *International Journal of Plasticity,* 19**,** 1297-1319.

BARLAT, F., FERREIRA DUARTE, J. M., GRACIO, J. J., LOPES, A. B. & RAUCH, E. F. 2003b. Plastic flow for non-monotonic loading conditions of an aluminum alloy sheet sample. *International Journal of Plasticity,* 19**,** 1215-1244.

BARLAT, F., MAEDA, Y., CHUNG, K., YANAGAWA, M., BREM, J. C., HAYASHIDA, Y., LEGE, D. J., MATSUI, K., MURTHA, S. J., HATTORI, S., BECKER, R. C. & MAKOSEY, S. 1997. Yield function development for aluminum alloy sheets. *Journal of the Mechanics and Physics of Solids,* 45**,** 1727-1763.

BARRETT, C. & MASSALSKI, T. 1980. Structure of Metals (3rd rev. edn.) Pergamon Press. Oxford.

BASINSKI, Z., SZCZERBA, M., NIEWCZAS, M., EMBURY, J. & BASINSKI, S. 1997. The transformation of slip dislocations during twinning of copper-aluminum alloy crystals. *Revue de mEtallurgie,* 94**,** 1037-1044.

BATE, P. S., BROUGH, I. & MORSE, S. 2007. Static Recovery and the Orthogonal Strain Path Change Effect in IF Steel. *Materials Science Forum,* 550**,** 141-148.

BAUSCHINGER, J. 1881. Changes of the elastic limit and the modulus of elasticity on various metals. *Zivilingenieur,* 27**,** 289-348.

BISHOP, J. & HILL, R. 1951. XLVI. A theory of the plastic distortion of a polycrystalline aggregate under combined stresses. *The London, Edinburgh, and Dublin Philosophical Magazine and Journal of Science,* 42**,** 414-427.

BRICKENKAMP, W. 1983. *Kornvergrösserungstexturen und Kornwachstumskinetik in Kupfer-Legierungen.*

CHAPARRO, B. M. & FERNANDES, J. V. 2002. Taylor analysis for {111}〈112〉 twinning on one system and {111}〈110〉 slip under tension and compression flow conditions. *Key Engineering Materials.*

CHAPARRO, B. M., VIEIRA, M. M. & FERNANDES, J. V. 2004. Influence of the mechanical microtwinning on the plastic behaviour of the AISI 304 stainless steel. *Materials Science Forum.*

CHRISTIAN, J. W. & MAHAJAN, S. 1995. Deformation twinning. *Progress in Materials Science,* 39**,** 1-157.

CORRÊA, E. C. S., AGUILAR, M. T. P. & CETLIN, P. R. 2002. The effect of tension/torsion strain path changes on the work hardening of Cu–Zn brass. *Journal of Materials Processing Tech.,* 124**,** 384-388.

DIETER, G. E. 1961. *Mechanical metallurgy,* New York, McGraw-Hill.

DOUCET, A. B. & WAGONER, R. H. 1987. plane-strain work hardening and transient behavior of interstitial-free steel. *Metallurgical Transactions A,* 18**,** 2129-2134.

EARDLEY, E., SOULET, A., COURT, S. A., HUMPHREYS, F. & BATE, P. S. 2003. Microstructure and plastic anisotropy in rolled Al-Mg alloys. *Thermec'2003, Pts 1-5,* 426-4**,** 363-368.

EL-DANAF, E., KALIDINDI, S. R. & DOHERTY, R. D. 1999. Influence of grain size and stacking-fault energy on deformation twinning in fcc metals. *Metallurgical and Materials Transactions A,* 30**,** 1223-1233.

EL-DANAF, E., KALIDINDI, S. R., DOHERTY, R. D. & NECKER, C. 2000. Deformation texture transition in brass: critical role of micro-scale shear bands. *Acta Materialia,* 48**,** 2665-2673.

FEAUGAS, X. 1999. On the origin of the tensile flow stress in the stainless steel AISI 316L at 300 K: back stress and effective stress. *Acta Materialia,* 47**,** 3617-3632.

FERNANDES, J. V. & SCHMITT, J. H. 1983. Dislocation microstructures in steel during deep drawing. *Philosophical Magazine A,* 48**,** 841-870.

FRANCIOSI, P., STOUT, M., O'ROURKE, J., ERSKINE, B. & KOCKS, U. 1987. Channel die tests on Al and Cu polycrystals: Study of the prestrain history effects on further large strain texture. *Acta Metallurgica,* 35**,** 2115-2128.

GOTTSTEIN, G. & SHVINDLERMAN, L. S. 2009. *Grain boundary migration in metals: thermodynamics, kinetics, applications,* CRC press.

GRACIO, J. J., FERNANDES, J. V. & SCHMITT, J. H. 1989. Effect of grain size on substructural evolution and plastic behaviour of copper. *Materials Science and Engineering A,* 118**,** 97-105.

HA, J., KIM, J.-H., BARLAT, F. & LEE, M.-G. 2014. Continuous strain path change simulations for sheet metal. *Computational Materials Science,* 82**,** 286-292.

HERSHEY, A. 1954. The plasticity of an isotropic aggregate of anisotropic face-centered cubic crystals. *Journal of Applied Mechanics-Transactions of the Asme,* 21**,** 241-249.

HILL, R. 1948. A Theory of the Yielding and Plastic Flow of Anisotropic Metals. *Proceedings of the Royal Society of London. Series A, Mathematical and Physical Sciences (1934-1990),* 193**,** 281-297.

HILL, R. 1990. Constitutive modelling of orthotropic plasticity in sheet metals. *Journal of the Mechanics and Physics of Solids,* 38**,** 405-417.

HIRSCH, J. & LÜCKE, K. 1988a. Overview no. 76: Mechanism of deformation and development of rolling textures in polycrystalline fcc metals—I. Description of rolling texture development in homogeneous CuZn alloys. *Acta Metallurgica,* 36**,** 2863-2882.

HIRSCH, J. & LÜCKE, K. 1988b. Overview no. 76: Mechanism of deformation and development of rolling textures in polycrystalline fcc metals—II. Simulation and interpretation of experiments on the basis of Taylor-type theories. *Acta Metallurgica,* 36**,** 2883-2904.

HOSFORD, W. F. 1985. Comments on anisotropic yield criteria. *International Journal of Mechanical Sciences,* 27**,** 423-427.

HU, H., CLINE, R. & GOODMAN, S. 1966. Deformation textures of metals. *Recrystallization, Grain Growth and Textures***,** 295-374.

HUTCHINSON, W. B., ARTHEY, R. & MALMSTRÖM, P. 1976. On anomalously low work-hardening in pre-strained metals. *Scripta Metallurgica,* 10**,** 673-675.

HÅGENSEN, T. A. 2016. Strain-Path Changes in Brass (CuZn20). Unpublished Specialization Project. Trondheim, Norway: The Norwegian University of Science and Technology.

IKEDA, S. 1972. Continuous observation of cell-formation in iron foils extended in an electron microscope. *Japanese Journal of Applied Physics,* 11**,** 1273.

KALIDINDI, S. R., SALEM, A. A. & DOHERTY, R. D. 2003. Role of deformation twinning on strain hardening in cubic and hexagonal polycrystalline metals. *Advanced Engineering Materials,* 5**,** 229-232.

KARAMAN, I., SEHITOGLU, H., CHUMLYAKOV, Y. & MAIER, H. 2002. The deformation of low-stacking-fault-energy austenitic steels. *JOM,* 54**,** 31.

KAWASAKI, Y. & TAKEUCHI, T. 1980. Cell structures in copper single crystals deformed in the [001] and [111] axes. *Scripta Metallurgica,* 14**,** 183-188.

KOCKS, U., CHEN, H. & RIGNEY, D. Strain hardening phenomenon of low stacking fault energy material in tensile test [C] AIME Met. Conference. Serminar, 1981. 151-175.

KOCKS, U. F. & CHANDRA, H. 1982. Slip geometry in partially constrained deformation. *Acta Metallurgica,* 30**,** 695-709.

KORBEL, A., DOBRZANSKI, F. & RICHERT, M. 1983. Strain hardening of aluminium at high strains. *Acta Metallurgica,* 31**,** 293-298.

KORBEL, A. & MARTIN, P. 1988. Microstructural events of macroscopic strain localization in prestrained tensile specimens. *Acta Metallurgica*, 36**,** 2575-2586.

KRÖNER, E. 1958. Berechnung der elastischen Konstanten des Vielkristalls aus den Konstanten des Einkristalls. *Zeitschrift für Physik,* 151**,** 504-518.

LAHAIE, D., EMBURY, J. D., CHADWICK, M. M. & GRAY, G. T. 1992. A note on the deformation of fine grained magnesium alloys. *Scripta Metallurgica et Materialia,* 27**,** 139-142.

LANKFORD, W., SNYDER, S. & BAUSCHER, J. 1950. New criteria for predicting the press performance of deep drawing sheets. *Trans. ASM,* 42**,** 1197-1205.

LEBENSOHN, R. A. & TOMÉ, C. N. 1994. A self-consistent viscoplastic model: prediction of rolling textures of anisotropic polycrystals. *Materials Science and Engineering: A,* 175**,** 71-82.

LEE, W.-S. & LIN, C.-F. 2002. Comparative study of the impact response and microstructure of 304L stainless steel with and without prestrain. *Metallurgical and Materials Transactions A,* 33**,** 2801-2810.

LI, F. & BATE, P. S. 1991. Strain path change effects in cube textured aluminium sheet. *Acta Metallurgica Et Materialia,* 39**,** 2639-2650.

LORETTO, M. H., CLAREBROUGH, L. M. & SEGALL, R. L. 1965. Stacking-fault tetrahedra in deformed face-centred cubic metals. *Philosophical Magazine,* 11**,** 459-465.

LUFT, A. 1991. Microstructural processes of plastic instabilities in strengthened metals. *Progress in Materials Science,* 35**,** 97-204.

MÁNIK, T., HOLMEDAL, B. & HOPPERSTAD, O. S. 2015. Strain-path change induced transients in flow stress, work hardening and r-values in aluminum. *International Journal of Plasticity,* 69**,** 1-20.

MCQUEEN, H., BAILON, J. P. & DICKSON, J. 2016. *Strength of Metals and Alloys (ICSMA 7): Proceedings of the 7th International Conference on the Strength of Metals and Alloys, Montreal, Canada, 12–16 August 1985,* Elsevier.

MECKING, H. & KOCKS, U. 1981. Kinetics of flow and strain-hardening. *Acta Metallurgica,* 29**,** 1865-1875.

MISES, R. V. 1913. Mechanik der festen Körper im plastisch-deformablen Zustand. *Nachrichten von der Gesellschaft der Wissenschaften zu Göttingen, Mathematisch-Physikalische Klasse,* 1913**,** 582-592.

OROWAN, E. 1959. Causes and Effects of Internal Stresses. *In:* RASSWEILER, G. M. & GRUBE, W. L. (eds.) *Internal Stresses and Fatigue in Metals.* New York: Elsevier Pub. Co.

PAUL, H., DRIVER, J. H. & JASIEŃSKI, Z. 2002. Shear banding and recrystallization nucleation in a Cu–2%Al alloy single crystal. *Acta Materialia,* 50**,** 815-830.

PROUST, G., KASCHNER, G. C., BEYERLEIN, I. J., CLAUSEN, B., BROWN, D. W., MCCABE, R. J. & TOMÉ, C. N. 2010. Detwinning of High-Purity Zirconium: In-Situ Neutron Diffraction Experiments. *Experimental Mechanics,* 50**,** 125-133.

RAPHANEL, J. L., SCHMITT, J. H. & BAUDELET, B. 1986. Effect of a prestrain on the subsequent yielding of low carbon steel sheets: experiments and simulations. *International Journal of Plasticity,* 2**,** 371-378.

RAUCH, E. F. 1997. The stresses and work hardening rates of mild steel with different dislocation patterns. *Materials Science & Engineering A,* 234**,** 653-656.

RAUCH, E. F. & SCHMITT, J. H. 1989. Dislocation substructures in mild steel deformed in simple shear. *Materials Science and Engineering: A,* 113**,** 441-448.

ROMHANJI, E., MILENKOVIC, V. & DROBNJAK, D. 1992. The grain size and alloying influence on the strain hardening of polycrystalline α-brasses. *Zeitschrift für Metallkunde,* 83**,** 110-114.

SACHS, G. 1928. Plasticity problems in metals. *Transactions of the Faraday Society,* 24**,** 84-92.

SAKHAROVA, N. A., FERNANDES, J. V. & VIEIRA, M. F. 2009. Strain path and work-hardening behavior of brass. *Materials Science & Engineering A,* 507**,** 13-21.

SAKHAROVA, N. A., VIEIRA, M. M., FERNANDES, J. V. & VIEIRA, M. F. 2008. Strain Path Change Effect on Deformation Behaviour of Materials with Low-to-Moderate Stacking Fault Energy. *In:* MARQUES, A. T., SILVA, A. F., BAPTISTA, A. P. M.,

SA, C., ALVES, F., MALHEIROS, L. F. & VIEIRA, M. (eds.) *Advanced Materials Forum Iv.* Stafa-Zurich: Trans Tech Publications Ltd.

SALEM, A. A., KALIDINDI, S. R. & DOHERTY, R. D. 2003. Strain hardening of titanium: role of deformation twinning. *Acta Materialia,* 51**,** 4225-4237.

SCHMITT, J. H., AERNOUDT, E. & BAUDELET, B. 1985. Yield loci for polycrystalline metals without texture. *Materials Science and Engineering,* 75**,** 13-20.

SCHMITT, J. H., FERNANDES, J. V., GRACIO, J. J. & VIEIRA, M. F. 1991. Plastic behaviour of copper sheets during sequential tension tests. *Materials Science & Engineering A,* 147**,** 143-154.

SOMEKAWA, H. & MUKAI, T. 2013. Hall–Petch relation for deformation twinning in solid solution magnesium alloys. *Materials Science and Engineering: A,* 561**,** 378-385.

SONG, S. & GRAY, G. 1995. Influence of temperature and strain rate on slip and twinning behavior of Zr. *Metallurgical and materials Transactions A,* 26**,** 2665-2675.

SUWAS, S. & RAY, R. K. 2014. *Crystallographic Texture of Materials,* London, Springer London, London.

SZCZEPIŃSKI, W. & MIASTKOWSKI, J. 1968. An experimental study of the effect of the prestraining history on the yield surfaces of an aluminium alloy. *Journal of the Mechanics and Physics of Solids,* 16**,** 153-162.

TAYLOR, G. I. & QUINNEY, H. 1932. The Plastic Distortion of Metals. *Philosophical Transactions of the Royal Society of London. Series A, Containing Papers of a Mathematical or Physical Character,* 230**,** 323-362.

THUILLIER, S. & RAUCH, E. F. 1994. Development of microbands in mild steel during cross loading. *Acta Metallurgica et Materialia,* 42**,** 1973-1983.

TRESCA, H. 1864. Memoire sur l'écoulement des solides à de forte pressions. *Acad. Sci. Paris,* 2**,** 59.

VAN HOUTTE, P. 1988. A Comprehensive Mathematical Formulation of an Extended Taylor–Bishop–Hill Model Featuring Relaxed Constraints, the Renouard–Wintenberger Theory and a Strain Rate Sensitivity Model. *Textures and Microstructures,* 8**,** 313-350.

VAN HOUTTE, P., DELANNAY, L. & SAMAJDAR, I. 1999. Quantitative Prediction of Cold Rolling Textures in Low-Carbon Steel by Means of the Lamel Model. *Textures and Microstructures,* 31**,** 109-149.

VAN HOUTTE, P., LI, S., SEEFELDT, M. & DELANNAY, L. 2005. Deformation texture prediction: from the Taylor model to the advanced Lamel model. *International Journal of Plasticity,* 21**,** 589-624.

VENABLES, J. A. 1964. The nucleation and propagation of deformation twins. *Journal of Physics and Chemistry of Solids,* 25**,** 693-700.

VIEIRA, M. F., SCHMITT, J. H., GRACIO, J. J. & FERNANDES, J. V. 1990. The effect of strain path change on the mechanical behaviour of copper sheets. *Journal of Materials Processing Tech.,* 24**,** 313-322.

VIEIRA, M. M., CHAPARRO, B. M., VIEIRA, M. F. & FERNANDES, J. V. 2004. Microstructural plastic behaviour of AISI 304 austenltic stainless steel.

VINCZE, G., RAUCH, E. F., GRACIO, J. J., BARLAT, F. & LOPES, A. B. 2005. A comparison of the mechanical behaviour of an AA1050 and a low carbon steel deformed upon strain reversal. *Acta Materialia*, 53**,** 1005-1013.

WAGNER, P., ENGLER, O. & LÜCKE, K. 1995. Formation of Cu-type shear bands and their influence on deformation and texture of rolled f.c.c. {112}〈111〉 single crystals. *Acta Metallurgica et Materialia,* 43**,** 3799-3812.

WRÓBEL, M., DYMEK, S. & BLICHARSKI, M. 1996. The effect of strain path on microstructure and texture development in copper single crystals with (110)[001]and (110)[11̄0]initial orientations. *Scripta Materialia,* 35**,** 417-422.

ZANDRAHIMI, M., PLATIAS, S., FRICE, D., BARRETT, D., BATE, P. S. & ROBERTS, W. T. 1989. Effects of changes in strain path on work hardening in cubic metals. *Metallurgical Transactions A,* 20**,** 2471-2482.

ZHANG, K., HOLMEDAL, B., HOPPERSTAD, O. S., DUMOULIN, S., GAWAD, J., VAN BAEL, A. & VAN HOUTTE, P. 2015. Multi-level modelling of mechanical anisotropy of commercial pure aluminium plate: Crystal plasticity models, advanced yield functions and parameter identification. *International Journal of Plasticity,* 66**,** 3-30.

Appendix A - Yld2004-18d

```
% clear all
clc

% ************** fitting method **************** %
% 1 for fitting to yield stress and R-values
% 2 for fitting to stress states at different strain paths
% 3 for fitting to both data in 1 and 2
% 4 just for plot purpose
% 5 Fitting to stress points as well as strain directions
fitmod = 1

% **************** Initial guess ***************** %
if fitmod ==1

disp('!!**********************************************************!!
!!')
disp('!!   Task Name:  Fit to Experimental points, AA1050-CALAMEL
FOR BIAXIAL       !!')
x0 = ones(14,1);
end

if fitmod ==2

disp('!!**********************************************************!!
!!')
disp('!!   Task Name:  Fit to FC_TAYLOY 201      POINTS
!!')
disp('!!   Must check the STRESS-POINTS FILE NAME in fitprog2
!!')
disp('      CALAMEL Type III Fitting with a = 6
')
disp('!!   Check weighting factors for sigmabar, typical 20
!!')
disp('!!**********************************************************!!
!!')
x0 = ones(14,1);
%   x0(19) = 8.0;
end

if fitmod ==7
  disp('!!************************************************!!')
disp('!! Task Name:  Fit to FC+TAYLOY 201 POINTS!!')
disp('!! Must check the STRESS-POINTS FILE NAME in fitprog2!!')
disp('  CALAMEL Type III Fitting with a = 6')
disp('!! Check weighting factors for sigmabar, typical 20!!')
disp('!!**********************************************!!')
x0 = ones(14,1);
% x0(19) = 8.0;
end

if fitmod ==3
```

```
  disp('!!************************************************!!!!')
disp('!!Task Name:  FIT TO EXP+ ALAMEL3. NormalisedStress VPSC-
matlab.txt!!')
disp('!! Must check the STRESS-POINTS FILE NAME in fitprog3!!')
disp('!!Check weighting factors for YS, typical 1, R 0.25!!')
disp('!!   5D STRESS 0.04,  Sigmabar 10!!')
disp('!!**************** ******************************!!!!')
x0 = ones(18,1);
end

% In this mode, the exponent is also fitted
if fitmod ==4
  x0 = ones(19,1);
  x0(19) = 10 ;
end

% Both stress as well as strain direction are both used
if fitmod == 5
%  x0 = ones(18,1);
end

% ***************** SOLVER ********************** %
% options = optimset('Algorithm',{'levenberg-
marquardt',0.01},'MaxIter',100000,'MaxFunEvals',100000,'TolFun',1e-
10,'TolX',1e-10);
options = optimset('Algorithm',{'levenberg-
marquardt',0.001},'MaxIter',30000,'MaxFunEvals',20000,'TolFun',1e-
11,'TolX',1e-11);

if fitmod==1
disp('Fit to Yield Stress and R-values!')
disp(clock);
tic;
[x,resnorm,residual,exitflag,output] =
lsqnonlin(@fitprog1,x0,[],[],options)
disp(clock);
toc;
end

if fitmod==2
disp('Fit to stress states !')
disp('Note: The order of stress states is by Vigot notion!')
disp(clock);
tic;
[x,resnorm,residual,exitflag,output] =
lsqnonlin(@fitprog2,x0,[],[],options)
disp(clock);
toc;
end


if fitmod==3
disp('Fit to stress states as well as Yield Stress and R-values!')
disp(clock);
tic;
```

```
[x,resnorm,residual,exitflag,output] =
lsqnonlin(@fitprog3,x0,[],[],options)
disp(clock);
toc;
end

if fitmod==4
disp('Fit to stress states, m is also fitted !')
disp('Note: The order of stress states is by Vigot notion!')
x0(19)
disp(clock);
tic;
[x,resnorm,residual,exitflag,output] =
lsqnonlin(@fitprog2,x0,[],[],options)
disp(clock);
toc;
end

if fitmod == 5
 disp('Fit to stress states and strain rate directional!')
 disp(' CALAMEL and 201 points, a = 6')
 disp('Note: The order of stress states is by Vigot notion!')
 disp(clock);
 tic;
 [x,resnorm,residual,exitflag,output] =
lsqnonlin(@fitprog5,x0,[],[],options)
 disp(clock);
 toc;
end

if fitmod == 6
 disp('Fit the exponent N of the Yield functions!')
 n0 = 6;
 tic;
 [n,resnorm,exitflag,output] = lsqnonlin(@fitprog6,n0,[],[],options)
 toc;
end


if fitmod==7
disp('Fit to stress states !')
disp('Note: The order of stress states is by Vigot notion!')
disp('Note: Not add the constraints on RD00, instead rescale it!')
disp(clock);
tic;
[x,resnorm,residual,exitflag,output] =
lsqnonlin(@fitprog7,x0,[],[],options)
disp(clock);

% Sig0=[1 0 0;0 0 0;0 0 0];
% sig_bar = yld2004_eqS(Sig0);
% xtmp = x;
% if sig_bar>=1.0
%  x = xtmp*sig_bar;
% else
%  x = xtmp/sig_bar;
```

```
% end

toc;
end

if fitmod == 8
 disp('Fit the exponent N of the Yield functions!')
 n0 = [8 1];
 tic;
 [n,resnorm,exitflag,output] = lsqnonlin(@fitprog8,n0,[],[],options)
 toc;
end
```

```
function F = fitprog1(coef)

global  c12 c13 c21 c23 c31 c32 ...
        c44 c55 c66 d12 d13 d21 d23 ...
        d31 d32 d44 d55 d66 m

% ####  Coefficients Initialisation  ####%
if length(coef) == 18
% All coefficient are going to be fitted
    c12 = coef(1);
    c13 = coef(2);
    c21 = coef(3);
    c23 = coef(4);
    c31 = coef(5);
    c32 = coef(6);
    c44 = coef(7);
    c55 = coef(8);
    c66 = coef(9);
    d12 = coef(10);
    d13 = coef(11);
    d21 = coef(12);
    d23 = coef(13);
    d31 = coef(14);
    d32 = coef(15);
    d44 = coef(16);
    d55 = coef(17);
    d66 = coef(18);
elseif length(coef) == 14
%     Coefficients govern out of plane properties are set to 1.0
    c12 = coef(1);
    c13 = coef(2);
    c21 = coef(3);
    c23 = coef(4);
    c31 = coef(5);
    c32 = coef(6);
    c44 = 1;
    c55 = 1;
    c66 = coef(7);
    d12 = coef(8);
    d13 = coef(9);
    d21 = coef(10);
```

```
    d23 = coef(11);
    d31 = coef(12);
    d32 = coef(13);
    d44 = 1;
    d55 = 1;
    d66 = coef(14);
else warning('Inconsistent coefficients')
end

% ### Initalise Parameters for fitting to Yield stress and R-values
### %
 %******  Input variables  ******%
 m = 8;          %Exponent of yield function
 noEXP = 7;      %number of tensile tests
 noBEXP = 1;
 weightY0 = sqrt(1);     %weight factor for Ys at RD degree
 weightR =  sqrt(0.1);  %Weight factor for R-values
 weightB =  sqrt(0.05);  %Weight factor for biaxial test YS
 weightBR =  sqrt(0.01);  %Weight factor for biaxial test R
 %  weightBR  =  sqrt(0.01); %Weight factor for biaxial test R-value
 %*Input Yield stress and R-value from 0-90 degrees at noEXP
directions
 %*Note that the Yield stresses are normailised by value at 0 degree
 %*ydata(2noExp,1) contains the data to fit; first noExp are yield
stresses
 %*at diffrent direction from 0-90;the second half are R-values


% BRASS 20%
ydata = [1 %normalized yield stress 0
0.99347 %normalized yield stress 15
0.97805 %normalized yield stress 30
0.96755 %normalized yield stress 45
0.97967 %normalized yield stress 60
0.99661 %normalized yield stress 75
1.00889 %normalized yield stress 90
1.02814 %normalized yield stress biaxial
0.901 % R-value 0
0.994 % R-value 15
1.047 % R-value 30
1.121 % R-value 45
1.101 % R-value 60
1.054 % R-value 75
1.040 % R-value 90
1.15037 % R-value biaxial
];


  if max(size(ydata)) ~= 2*(noEXP+noBEXP)
    warning('Inconsistent number of directions!')
  end

% ### Calculatin of Y and R using current coefficient values ### %
xdata = zeros(2*(noEXP+noBEXP),1);
j = 1;
```

```
for angle = 0:(90/(noEXP-1)):90
    [r sigma11] = uniten_yld(angle,'yld2004');
    xdata(j)     = sigma11;
    xdata(noEXP+noBEXP+j) = r;
    j = j+1;
end

if noBEXP>0
[r sigma11] = biten_yld('yld2004');
xdata(noEXP+noBEXP)=sigma11;
xdata(2*(noEXP+noBEXP))=r;
end

% xdata(1:noEXP) = xdata(1:noEXP)/xdata(1);
% [r s11 s12] = testing(0,'biaxial');
% xdata(2*noTT+1)=r;

% ### Calculatin of residuals  ### %
% weightY0 = sqrt(1);
% weightR = sqrt(0.05);

if noBEXP == 0
    ww = [weightY0*ones(noEXP,1); weightR*ones(noEXP,1)];
else
ww = [weightY0*ones(noEXP,1);weightB;
weightR*ones(noEXP,1);weightBR];
end
F = zeros(2*(noEXP+noBEXP),1);
F = ww.*(xdata./ydata - 1);

% kai added on 19/12/2012 to make equivalent stress equal to 1 to
tensile at RD 00
sig23 = 0;
sig13 = 0;
sig12 = 0;
Sig0=[1 sig12 sig13;sig12 0 sig23;sig13 sig23 0];
sig_bar = yld2004_eqS(Sig0);
F(2*(noEXP+noBEXP)+1)  = sqrt(10)*(1-sig_bar);
F
F;
```

```
function [r,s11] = uniten_yld(angle,yldname)
% Compute R value, Stress factor at 'angle' degree to RD direction,
using the spcified
% yield function.
global m

% change angle from degree to radian
angle = angle*pi/180;

SigAng = [cos(angle)^2  sin(angle)*cos(angle)  0;...
          sin(angle)*cos(angle)  sin(angle)^2   0;...
          0  0  0];

% Calculate yield stress
```

```
switch yldname
    case 'yld2004'
      % yield stress at 0 degree
       Sig0=[1 0 0;0 0 0;0 0 0];
       sig_bar = yld2004_eqS(Sig0);
      % at angle phi
       fphi = yld2004_m(SigAng);
       sigYphi = (4/fphi)^(1/m);
       s11 = sigYphi*sig_bar;
      % Calculate R-value
       sG = s11*[cos(angle)^2  sin(angle)*cos(angle) 0;...
                     sin(angle)*cos(angle) sin(angle)^2  0;...
                     0 0 0];
       Sig0=[1 0 0;0 0 0;0 0 0];
       eqvS = yld2004_m(Sig0);
       difz = pd_yld(sG,3,1,'yld2004');
       r = -1-(m*eqvS)/(s11*difz);
       difx =  pd_yld(sG,1,1,'yld2004');
%        r = -1-difx/difz;
%        r2=r1-r

%        difx= pd_yld(sG,1,1,'yld2004');
%        dify = pd_yld(sG,2,1,'yld2004');
%        r2 = dify/-(difx+dify) ;
%        if abs(r2-r)> 0.1
%          disp('big difference for R');
%        end
end
```

```
function eqSyld2004 = yld2004_eqS(stress)
% Calculate the Eqivalent Stress of YLD2004-18P. Eqs =
% (0.25*PHI(Sig))^(1/m). This is in Vigot vector notation, i.e.
sig11,
% 22,33,23,13,12. The input is stress states.
global  c12 c13 c21 c23 c31 c32 ...
        c44 c55 c66 d12 d13 d21 d23 ...
        d31 d32 d44 d55 d66 m

    phi = yld2004_m(stress);
    eqSyld2004 = (phi/4.0)^(1/m);
```

```
function fyld2004_m_phi = yld2004_m(stress)
% Calculate the plastic potential using YLD2004-18P
% PHI(s)=(s1'-s1'')^m+...
% This is in Vigot vector notation, i.e. sig11,22,33,23,13,12.
% The input is stress states.

global  c12 c13 c21 c23 c31 c32 ...
        c44 c55 c66 d12 d13 d21 d23 ...
        d31 d32 d44 d55 d66 m

     t1 = stress(1,1);
```

```
     t2 = stress(2,2);
     t3 = stress(3,3);
     t4 = stress(2,3);
     t5 = stress(3,1);
     t6 = stress(1,2);
%      t4 = stress(1,2);
%      t5 = stress(2,3);
%      t6 = stress(3,1);


% ***************************************************************
% * CIJ is the first transformation matrix, DIJ is the second   *
% * Transformation matrix, M is the exponent, T is the stress   *
% * Components                                                  *
% ***************************************************************

      L111 = (c12 + c13) * 1/3;
      L112 = (c13 - 2 * c12) * 1/3;
      L113 = (c12 - 2 * c13) * 1/3;
      L121 = (c23 - 2 * c21) * 1/3;
      L122 = (c21 + c23) * 1/3;
      L123 = (c21 - 2 * c23) * 1/3;
      L131 = (c32 - 2 * c31) * 1/3;
      L132 = (c31 - 2 * c32) * 1/3;
      L133 = (c31 + c32) * 1/3;

      L211 = (d12 + d13) * 1/3;
      L212 = (d13 - 2 * d12) * 1/3;
      L213 = (d12 - 2 * d13) * 1/3;
      L221 = (d23 - 2 * d21) * 1/3;
      L222 = (d21 + d23) * 1/3;
      L223 = (d21 - 2 * d23) * 1/3;
      L231 = (d32 - 2 * d31) * 1/3;
      L232 = (d31 - 2 * d32) * 1/3;
      L233 = (d31 + d32) * 1/3;

% Finds the deviatoriske components of the transformed stress
      s11 = L111 * t1 + L112 * t2 + L113 * t3;
      s12 = L121 * t1 + L122 * t2 + L123 * t3;
      s13 = L131 * t1 + L132 * t2 + L133 * t3;
      s14 = c44 * t4;
      s15 = c55 * t5;
      s16 = c66 * t6;

      s21 = L211 * t1 + L212 * t2 + L213 * t3;
      s22 = L221 * t1 + L222 * t2 + L223 * t3;
      s23 = L231 * t1 + L232 * t2 + L233 * t3;
      s24 = d44 * t4;
      s25 = d55 * t5;
      s26 = d66 * t6;

% Finner egenverdiene
      h11 = (s11 + s12 + s13) * 1/3;
      h21 = (s21 + s22 + s23) * 1/3;

      h12 = 1/3 * (s15 * s15 + s16 * s16 + s14 * s14 ...
```

```
         - s12 * s13 - s13 * s11 - s11 * s12);
      h22 = 1/3 * (s25 * s25 + s26 * s26 + s24 * s24 ...
         - s22 * s23 - s23 * s21 - s21 * s22);

      h13 = (2 * s15 * s16 * s14 + s11 * s12 * s13 ...
         - s11 * s14 * s14 - s12 * s15 * s15 ...
         - s13 * s16 * s16) * 0.5;
      h23 = (2 * s25 * s26 * s24 + s21 * s22 * s23 ...
         - s21 * s24 * s24 - s22 * s25 * s25 ...
         - s23 * s26 * s26) * 0.5;

      p1 = (h11 * h11 + h12);
      p2 = (h21 * h21 + h22);
      q1 = (2 * h11^3 + 3 * h11 * h12 + 2 * h13) ...
        * 0.5;
      q2 = (2 * h21^3 + 3 * h21 * h22 + 2 * h23) ...
        * 0.5;

% Oringal version, ftrom Gryten.
      if (p1 > 0) && (p1^1.5 > abs(q1))
            theta1 = atan(-q1 / p1^1.5 / ...
                    sqrt(-q1 / p1^1.5 * ...
                    q1 / p1^1.5 + 1)) + 2 * ...
                   atan(1);
            s11 = 2 * sqrt(h11 * h11 + h12) * cos(theta1 * 1/3) ...
                 + h11;
            s12 = 2 * sqrt(h11 * h11 + h12) * ...
                 cos((theta1 + 4 * pi) * 1/3) + h11;
            s13 = 2 * sqrt(h11 * h11 + h12) * ...
                 cos((theta1 + 2 * pi) * 1/3) + h11;
      elseif (p1 > 0) && (p1^1.5 <= abs(q1))
            if (q1 < 0)
                theta1 = pi;
            end
            if (q1 > 0)
                theta1 = 0;
            end
            s11 = 2 * sqrt(h11 * h11 + h12) * ...
                 cos(theta1 * 1/3) + h11;
            s12 = 2 * sqrt(h11 * h11 + h12) * ...
                 cos((theta1 + 4 * pi) * 1/3) + h11;
            s13 = 2 * sqrt(h11 * h11 + h12) * ...
                 cos((theta1 + 2 * pi) * 1/3) + h11;
      else
            s11 = h11;
            s12 = h11;
            s13 = h11;
      end

% % From paper F. Balart 2007
%       theta1 = acos(q1/(p1^1.5));
%       s11 = 2 * sqrt(h11 * h11 + h12) * cos(theta1 * 1/3) ...
%             + h11;
%       s12 = 2 * sqrt(h11 * h11 + h12) * ...
%             cos((theta1 + 4 * pi) * 1/3) + h11;
%       s13 = 2 * sqrt(h11 * h11 + h12) * ...
```

```
%             cos((theta1 + 2 * pi) * 1/3) + h11;

      if (p2 > 0) && (p2^1.5 > abs(q2))
            theta2 = atan(-q2 / p2^1.5 / ...
                    sqrt(-q2 / p2^1.5 * ...
                    q2 / p2^1.5 + 1)) + 2 * ...
                    atan(1);
            s21 = 2 * sqrt(h21 * h21 + h22) * cos(theta2 * 1/3) ...
                 + h21;
            s22 = 2 * sqrt(h21 * h21 + h22) * ...
                 cos((theta2 + 4 * pi) * 1/3) + h21;
            s23 = 2 * sqrt(h21 * h21 + h22) * ...
                 cos((theta2 + 2 * pi) * 1/3) + h21;
      elseif (p2 > 0) && (p2^1.5 <= abs(q2))
            if (q2 < 0)
                theta2 = pi;
            end
            if (q2 > 0)
                theta2 = 0;
            end
            s21 = 2 * sqrt(h21 * h21 + h22) * ...
                 cos(theta2 * 1/3) + h21;
            s22 = 2 * sqrt(h21 * h21 + h22) * ...
                 cos((theta2 + 4 * pi) * 1/3) + h21;
            s23 = 2 * sqrt(h21 * h21 + h22) * ...
                 cos((theta2 + 2 * pi) * 1/3) + h21;
      else
            s21 = h21;
            s22 = h21;
            s23 = h21;
      end

%             theta2 = acos(q2/(p2^1.5));
%             s21 = 2 * sqrt(h21 * h21 + h22) * cos(theta2 * 1/3)
...
%                  + h21;
%             s22 = 2 * sqrt(h21 * h21 + h22) * ...
%                  cos((theta2 + 4 * pi) * 1/3) + h21;
%             s23 = 2 * sqrt(h21 * h21 + h22) * ...
%                  cos((theta2 + 2 * pi) * 1/3) + h21;

      phi = abs(s11-s21)^m + abs(s11-s22)^m + abs(s11-s23)^m ...
         + abs(s12-s21)^m + abs(s12-s22)^m + abs(s12-s23)^m ...
         + abs(s13-s21)^m + abs(s13-s22)^m + abs(s13-s23)^m;

     fyld2004_m_phi = phi;

%      fyld2004_eqvs = (phi/4)^(1/m);
```

```
function pds = pd_yld(sG, dnum, modeflag,yldname)
% Calculate partial derivative of yield function plastic potential
function(modeflag=1) or
% YLD2004 equivalent stress(modeflag=2). Using Richadson deferred
approach
```

```
% to the limit method. yldname = {'yld2004',..}
% dnum - 1-6, calculate which stress componets's partial deriative,
in
% Vigot's notation

% Calculate df/dsG(zz)using subroutine from Fortran recipe
CON=1.4;
CON2=CON*CON;
BIG=1.e10;
NTAB=12;
SAFE=2.;
h = 0.15;

%       INTEGER i,j
%       REAL errt,fac,hh,a(NTAB,NTAB)
a=zeros(NTAB);

if h==0
    disp('h must be nonzero in dfridr');
    pause(100);
end

 hh=h;
%
faddh = func_pd(sG, dnum, h, modeflag,yldname);
fsubh = func_pd(sG, dnum, -h, modeflag,yldname);
%
 a(1,1)=(faddh-fsubh)/(2.0*hh);
 err=BIG;

   for i=2:NTAB
        hh=hh/CON;
        faddh = func_pd(sG, dnum, hh, modeflag,yldname);
        fsubh = func_pd(sG, dnum, -hh, modeflag,yldname);
        a(1,i)=(faddh-fsubh)/(2.0*hh);
        fac=CON2;
        for j=2:i
          a(j,i)=(a(j-1,i)*fac-a(j-1,i-1))/(fac-1.);
          fac=CON2*fac;
          errt=max(abs(a(j,i)-a(j-1,i)),abs(a(j,i)-a(j-1,i-1)));
          if (errt<err)
            err=errt;
            difx=a(j,i);
          end
        end
          if(abs(a(i,i)-a(i-1,i-1))>=SAFE*err)
            break
          end
   end

%    Check erros
if err>1.e-3
    disp('warning erro > 1.e-3');
%     pause(1);
%     pds = -9999;
%     return
```

```
end

if difx==0
    disp('df/dsGzz = 0, erro');
    pds =-9999;
    return
end

 pds = difx;

end


% new function for temparery cal
function func = func_pd(sG, dnum, h, modeflag,yldname)
% calculate f(x+h), embeded in pd_yld.m
 if modeflag==1
%
     switch dnum
         case 1
           sG(1,1) = sG(1,1)+h  ;
         case 2
           sG(2,2) = sG(2,2)+h;
         case 3
           sG(3,3) = sG(3,3)+h;
         case 4
           sG(2,3) = sG(2,3)+h;
           sG(3,2) = sG(3,2)+h;
         case 5
           sG(1,3) = sG(1,3)+h;
           sG(3,1) = sG(3,1)+h;
         case 6
           sG(1,2) = sG(1,2)+h;
           sG(2,1) = sG(2,1)+h;
     end
%
     switch yldname
        case 'yld2004'
          func = yld2004_m(sG);
     end

 elseif modeflag==2
    %
     switch dnum
         case 1
           sG(1,1) = sG(1,1)+h  ;
         case 2
           sG(2,2) = sG(2,2)+h;
         case 3
           sG(3,3) = sG(3,3)+h;
         case 4
           sG(2,3) = sG(2,3)+h;
           sG(3,2) = sG(3,2)+h;
         case 5
           sG(1,3) = sG(1,3)+h;
           sG(3,1) = sG(3,1)+h;
```

```
         case 6
           sG(1,2) = sG(1,2)+h;
           sG(2,1) = sG(2,1)+h;
     end
%
    switch yldname
        case 'yld2004'
          func = yld2004_eqs(sG);
    end

 else
   disp('modeflag must be 1 or 2!');
   return
 end

end
```

```
function [r, sig_b] = biten_yld(yldname)
% Calculate biaxial tension R-value and yield stress value
global m

sG_bi = [1 0 0; 0 1 0; 0 0 0];

switch yldname
    case 'yld2004'
     % yield stress at 0 degree
       Sig0=[1 0 0;0 0 0;0 0 0];
       sig_bar = yld2004_eqS(Sig0);
     %Calculate stress
       fphi = yld2004_m(sG_bi);
       sigYphi = (4/fphi)^(1/m);
       sig_b = sigYphi*sig_bar;
     % Calculate the R-values
      sG = sig_b*[1 0 0; 0 1 0; 0 0 0];
      difx = pd_yld(sG,1,1,'yld2004');
      dify = pd_yld(sG,2,1,'yld2004');
      r = dify/difx;

end
```

Appendix B – Calculating normalized yield stress and r-values

```
function fitplot(coef)

global  c12 c13 c21 c23 c31 c32 ...
        c44 c55 c66 d12 d13 d21 d23 ...
        d31 d32 d44 d55 d66 m iter sigma11_0

%%%%%%%%%%%%%%%%%%%%%%%%%%%%%%%%%%%%%%%%%%%%%%%%%%%%%%%%%%%%%%%%%%%%%

if length(coef) == 18
    c12 = coef(1);
    c13 = coef(2);
    c21 = coef(3);
    c23 = coef(4);
    c31 = coef(5);
    c32 = coef(6);
    c44 = coef(7);
    c55 = coef(8);
    c66 = coef(9);
    d12 = coef(10);
    d13 = coef(11);
    d21 = coef(12);
    d23 = coef(13);
    d31 = coef(14);
    d32 = coef(15);
    d44 = coef(16);
    d55 = coef(17);
    d66 = coef(18);
    m = 8;
elseif length(coef) == 14
    c12 = coef(1);
    c13 = coef(2);
    c21 = coef(3);
    c23 = coef(4);
    c31 = coef(5);
    c32 = coef(6);
    c44 = 1;
    c55 = 1;
    c66 = coef(7);
    d12 = coef(8);
    d13 = coef(9);
    d21 = coef(10);
    d23 = coef(11);
    d31 = coef(12);
    d32 = coef(13);
    d44 = 1;
    d55 = 1;
    d66 = coef(14);
    m = 8;

elseif length(coef) == 19
    c12 = coef(1);
    c13 = coef(2);
    c21 = coef(3);
```

```
    c23 = coef(4);
    c31 = coef(5);
    c32 = coef(6);
    c44 = coef(7);
    c55 = coef(8);
    c66 = coef(9);
    d12 = coef(10);
    d13 = coef(11);
    d21 = coef(12);
    d23 = coef(13);
    d31 = coef(14);
    d32 = coef(15);
    d44 = coef(16);
    d55 = coef(17);
    d66 = coef(18);
    m = coef(19);

else warning('Inconsistent coefficients')
end

m
noEXP = 7;   % number of exp data
noFIT = 91;  % number of fitted points

xdata = zeros(2*noFIT,1);
j = 1;
for angle = 0:(90/(noFIT-1)):90
    [r sigma11] = uniten_yld(angle,'yld2004');
    xdata(j)     = sigma11;
    xdata(noFIT+j)  = r;
    j = j+1;
end

[r_b sigma_b] = biten_yld('yld2004')
[r sig_bar] = uniten_yld(0,'yld2004')
% yield stress at 0 degree
Sig0=[1 0 0;0 0 0;0 0 0];
sig_bar = yld2004_eqS(Sig0)
% xdata(1:noFIT) = xdata(1:noFIT)/xdata(1);

% BRASS 20%Zn
ydata = [1 %normalized yield stress 0
0.995 %normalized yield stress 15
0.967 %normalized yield stress 30
0.952 %normalized yield stress 45
0.979 %normalized yield stress 60
0.996 %normalized yield stress 75
1.02  %normalized yield stress 90
%1.02814 %normalized yield stress biaxial
0.901 % R-value 0
0.994 % R-value 15
1.047 % R-value 30
1.121 % R-value 45
1.101 % R-value 60
1.054 % R-value 75
```

```
1.040 % R-value 90
%1.15037 % R-value biaxial
];


%
% filename = 'fitGR_stress.dat';
% fid = fopen(filename);
% fm  = textscan(fid, '%f %f %[^\n]');
% fclose(fid);
% for i=1:max(size(fm{1}))
% xinp1(i)         = fm{1}(i);
% yinp1(i)         = fm{2}(i);
% end
%
% filename = 'fitGR_rvalues.dat';
% fid = fopen(filename);
% fm  = textscan(fid, '%f %f %[^\n]');
% fclose(fid);
% for i=1:max(size(fm{1}))
% xinp2(i)         = fm{1}(i);
% yinp2(i)         = fm{2}(i);
% end

% ********** check
if max(size(ydata)) ~= 2*noEXP
    warning('Incorrect number of experimental data')
end

% F = (xdata./ydata - 1);
% F = sum(F.^2)
% xdata(1:noFIT);
hold on
% **************** plotting ***************** %
% xdata(1:2*noFIT)
subplot(2,1,1)
plot([0:(90/(noFIT-1)):90],xdata(1:noFIT),'k-')
hold on
plot([0:(90/(noEXP-1)):90],ydata(1:noEXP),'.r')
% plot(xinp1,yinp1,'.b')
xlabel('Angle (°)')
ylabel('Normalized yield stress')
% legend('fitted yld2004','exp')
subplot(2,1,2)
% figure;
plot([0:(90/(noFIT-1)):90],xdata(noFIT+1:2*noFIT),'k-')
hold on
plot([0:(90/(noEXP-1)):90],ydata(noEXP+1:2*noEXP),'.r')
% plot(xinp2,yinp2,'.b')
xlabel('Angle (°)')
ylabel('R-values')
% legend('fitted yld2004','exp')
```